5th BSME International Conference on Thermal Engineering

Topographical condition of mild steel after an orthogonal cutting

Kazi Md. Masum Billah*, Md. Maruf Hossain, Tarapada Bhowmick, Abdullah Al Bari

Department of Mechanical Engineering, Khulna University of Engineering & Technology, Khulna-9203, Bangladesh

Abstract

Now a days it is very common interest for engineers to improve the surface quality. Improvement of surface quality deals with several factors like cutting condition, heat generation, heat dissipation, selection of cutting fluid etc. Above all the factors it is very important to know about the change in microstructure and behavior of the material. The surface quality that is the change in microstructure greatly depends on the cutting condition and process which are taken on account earlier, each of which produce a surface with own characteristic topography. In this paper the topographical condition of a mild steel workpiece and chip is investigated and described. For this purpose an orthogonal cutting of mild steel metal with cutting tool of high speed metal is taken. The change in microstructure of chip and work material is observed in the metallurgical microscope. Then finally it is observed, the total change of microstructure of each surface held with the proportion of heat generation and distribution.

Keywords: Specimen topography; Heat generation; Heat dissipation; Microstructure

1. Introduction

For the production of variety metallic products metal removal operations are widely used in industry. During metal removal process the first objective is to obtain a smooth surface. The metal surface smoothness is greatly depends on the machining process. The basic principle of metal removal is that the heat generation between tool and work material contact surface with friction. The heat generation is closely related to the plastic deformation and friction [1]. It can be specified that three main source of heat during machining or cutting e.g. plastic deformation by shearing in the primary shear zone, plastic deformation by shearing and friction on the cutting face and friction between chip and tool on tool flank. The generated heat is mostly dissipated by discarded chip when no cutting fluid is used and the rest amount also draws away by cutting tool. The change in micro structure of mild steel interface occurs due to temperature. Different temperature distribution between chip and work material is observed [2]. By this observation it is shown that the amount of change in the different interface of mild steel with equally distribution of heat at different planes and faces. The microstructure analysis of the mild steel interfaces obtains by high speed cutting. In this work an orthogonal cutting of mild steel has done. Then the chip and work material topography observed at metallurgical microscope and compared with actual microstructure of mild steel. The paper is organized as follows, Experimental details provides the cutting technique, chip formation and process of taking image. The result section provides the microstructure images acquisition. Finally the comparison of topographical condition of mild steel and work experience is figured out in discussion and conclusion section.

---

* Corresponding author. Tel. +8801195037118
E-mail address: masum.me106@yahoo.com

2. **Experimental details**

The material examined was a mild steel specimen. Before setting for an orthogonal cutting the general topographical characteristics was observed in metallurgical microscope. And this also carried out by some steps which are not concerned matter of this work. The specimen then placed into a lathe machine for cutting at different speed and obtained the chip. The cutting was carried out at 700 rpm and 800 rpm. Then specimen and chips collected together for visualizing the topographical microstructure. The metallographic observations were carried out on both sample cut surface and chip. The microstructure features of the specimen and chip were characterized by optical and SEM observation. The metallurgical microscope was of Advanced Metallurgical Microscope type.
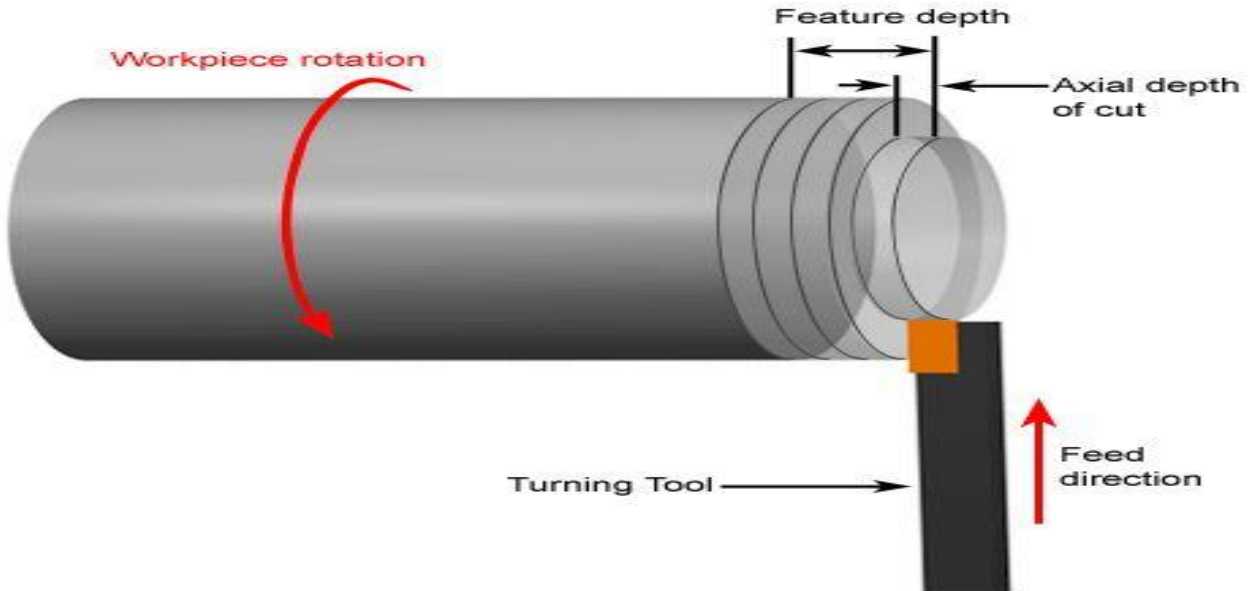

Fig.1. Typical orthogonal metal cutting

3. Results

Figure 2 shows the microstructure of mild steel specimen before cutting. It contains about .1% carbon in weight alloyed with iron. This steel has two major constituents, which are ferrite and pearlite. The light coloured region of the microstructure is ferrite. The grain boundaries between the ferrite grains can be seen quite clearly. The dark region is pearlite. It made up from a fine mixture of ferrite and iron carbide. The small spots within the ferrite grains could be exhibits. These are illusions and impurities such as oxide and sulphide.
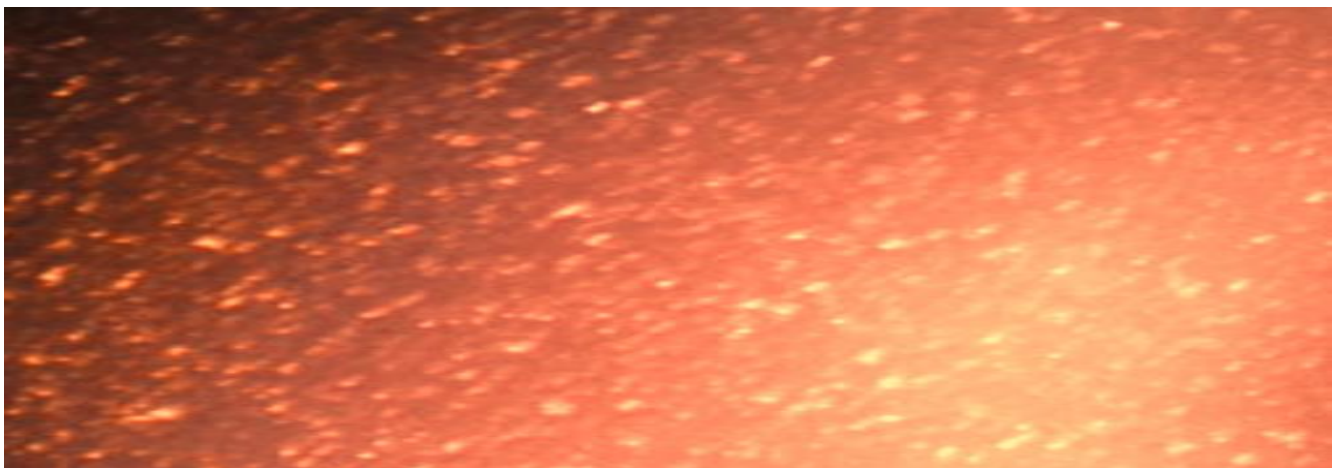

Fig. 2. Topographical microstructure of mild steel before cutting

The properties of mild steel greatly depend on the microstructure. Decreasing the size of the grains and decreasing the amount of pearlite develops the strength ductility and toughness of the steel. The inclusion can also affect the toughness. Figure 3 shows the topographical microstructure of the chip of mild steel after cutting. And figure 4 shows the microstructure of mild steel workpiece surface after cutting. The microstructure of the mild steel sample surface shows a rough structure of grained ferrite and pearlite with effect of bending and heat. Similarly in figure 3 also shows the rough structure of grain ferrite and pearlite with effect of bending and heat. According to the assumption of heat generation and distribution it is observed, the change in microstructure of chip is more affected by heat than the structure of workpiece surface. The microstructure changes observed are due to the fact that during cutting recrystalyzation and grain growths are interacting in a complex way to determine final grain size. The new grain size obviously disrupted by the heat which generated during cutting.
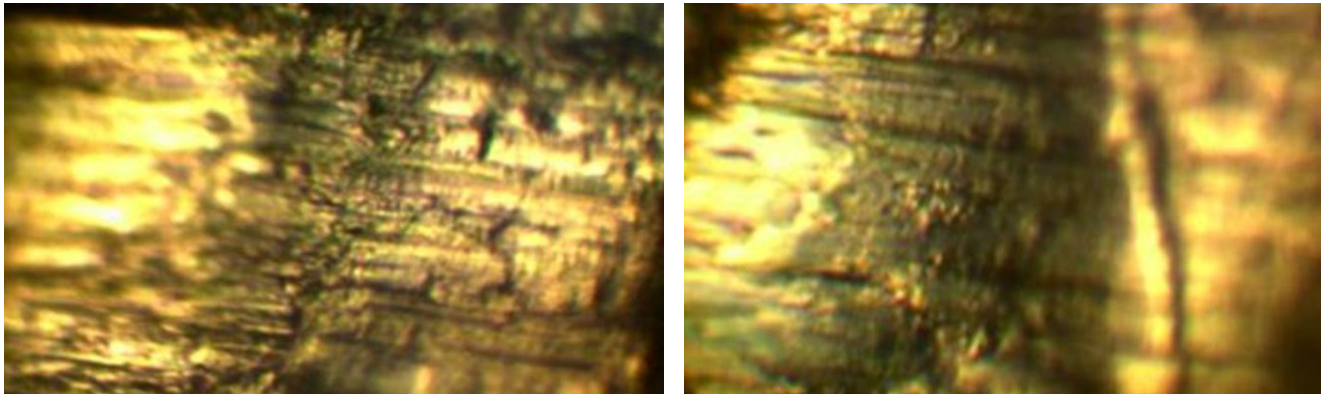

Fig. 3. Topographical microstructure of mild steel specimen after cutting

Fig. 4. Topographical microstructure of chip

4. Conclusion

This paper carried the use of imaging and pattern recognition techniques for the analysis of topographical microstructure of mild steel and its chip. The objective is to support research on influence on topographical microstructure in machining process. From this investigation it has been found that topographical microstructure of mild steel changes in different condition of cutting process. When the cutting speed was low, less crack and much black pearlite was formed compared to high speed condition. To optimize the surface characteristics additional cutting fluid should be provided during cutting. In future by a thermal imaging camera this investigation can be made so that it can attenuate the topographical microstructure of others metal more precisely.

References

[1] Valery Marinov, "Manufacturing Technology". Cutting Temperature, p.74

[2] Abukhsim, N. A., Sheikh, M. A., and Mativenga, P.T., 2006. "Heat generation temperature prediction in metal cutting: A review and implications for high speed machining". www.elsevier.com/locate/ijmactool, vol. 46, p. 782-800.

[3] Kisin, M., Noc Razinger, M., Pusavec, F., and Kopac, J., 2008. "Influence of temperature and microstructure of the workpiece material on energy quanta in cutting process". JAMME, vol. 30, issue 1.

[4] Shetty, R., Keni, L., Pai, P., and Kamath, V. 2008. "Experimental and analytical study on chip formation mechanism in machining of DRACs". APRN Journal of Engineering and Applied Sciences, vol.3, no. 5.

[5] Tyan, T., Yang, W. H., 1992. "Analysis of orthogonal metal cutting process". International journal for numerical methods in engineering, vol. 34, p. 365-389.

[6] Jam, J. E., and Fard, V. N., 2011. "A novel method to determine tool-chip thermal contact conductance in machining". IJEST, vol.3, no.12.

5ᵗʰ BSME International Conference on Thermal Engineering

Experimental analysis of wetting delay during jet impingement quenching of high temperature brass block

Md. Jubayer Hossain*, Md. Nazmul Hossain

Department of Mechanical Engineering, Bangladesh University of Engineering and Technology, Dhaka-1000, Bangladesh

Abstract

A model for the prediction of the wetting delay through jet impingement quenching of a high temperature brass block has been carried out in this study. The Liquids used for jet impingement on the brass surface are water and emulsion of cutting oil (used in machine shop) and water at a proportion of 1:20.The varying parameters used for the analysis are different velocities of jet (3m/s, 5m/s, 10m/s) and initial block temperature from 250°C to 450°C at an interval of 50°C. The wetting delay and wetting front propagation varied for different test conditions. When a liquid jet was impinged on the heated surface of the brass block, the jet remains stagnant up to a small region and the surface temperature decreases very slowly with time. After a certain interval, the surface temperature decreases at faster rate and the wetting front starts to move in the radial direction. The time that passes during the stagnant period of the wetting front is the wetting delay. The wetting delay in case of emulsion of cutting fluid is much higher as compared to water. The evidence was clear for wetting delay measurement for water from graphical analysis but for the emulsion it is not as evident as in many cases the temperature drops linearly with time and the wetting delay can't be actuated exactly. The water wave front propagates throughout the surface but in case of the emulsion the wetting front does not even cover half of the total metal surface after a long interval of time. The effect of different experimental parameters on the wetting delay is also observed in the present study. The characteristics of the wetting delay are influenced by jet velocity and initial block temperature. For higher jet velocity and lower initial block temperature wetting delay decreases.

Nomenclature		
d	Jet Diameter	(mm)
CHF	Critical Heat Flux	(W/m^2)
LFD	Leiden frost point	
t*	Resident time	(sec)
T_i	Initial Block Temperature	($^\circ$C)
V	Jet Velocity	(m/s)
T_w	Surface temperature	($^\circ$C)

* Corresponding author. Tel.:+88 01911 099149
E-mail address: hossain.jubayer@gmail.com

1. Introduction

The rapid cooling of high temperature metal surface is generally called quenching or rewetting process, which is one of the most important processes of heat treatment. Quenching is widely used and has been extensively studied for controlling the mechanical and metallurgical properties of materials in the manufacturing industry. Among the various quenching techniques, jet impingement quenching has been proved to be an effective cooling option over the past few years due to rapid cooling and better control of high temperatures. When a liquid jet is impinged on the heated surface of the metal block the surface is not immediately wetted by the liquid jet. The liquid jet remains stagnant up to a small region for a certain amount of time which may vary with the experimental conditions and the metal block we are using. At that time, the surface temperature decreases slowly almost at a constant rate. There is a sudden drop of temperature at the very beginning of jet impingement due to transient effect. After a certain amount of time the wave front of the jet begins to propagate on the whole surface. The delay of time when the wave front of jet remains stagnant on a small region of the surface is called wetting delay.
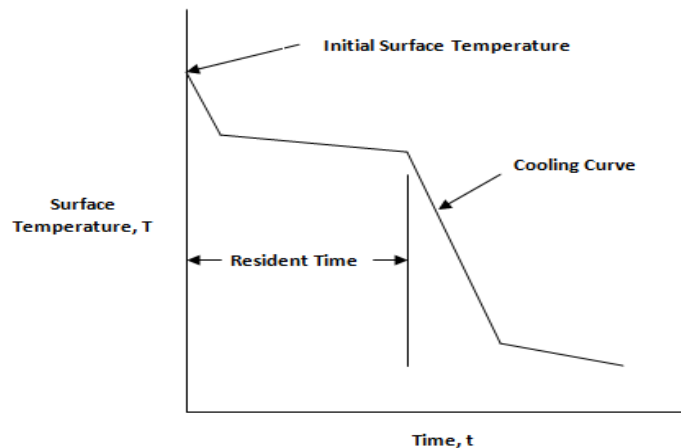

Fig. 1. Cooling curve during quenching

Researchers and scientists have carried out analytical and experimental investigations for clear understanding of quenching phenomena. Chan and Banerjee [1] defined that the rewetting is the re-establishment of continuous liquid contact with a hot dry surface. Nelson [2] defined quenching as the rewetting process for establishing direct liquid-solid contact where the surface initial temperature exceeds the rewetting temperature. The rewetting temperature was represented by the Leiden frost temperature (LDF) of liquid nitrogen on copper surface. The quenching by jet impingement using water as the liquid is a very effective cooling process for high temperature surfaces. Piggott et al. [3] experimentally investigated wetting delay during cooling of a hot rod using a sub cooled water jet. It is the delay of the wave front of the liquid to spread from a stagnant zone to the entire surface of the block. The time till when the wave front remains in a stagnant zone is called the resident time.

Mozumder et al. [4-6] conducted the experimental investigations during quenching of three different cylindrical blocks i.e. steel, brass, cast iron using a sub cooled water jet. The jet was impinged from the bottom at the center of the surface of the block. They defined resident time as the period required for the wetting front to expand beyond the stagnant zone which is close to the center.

The present study is of experimental type that is performed to understand the characteristics of wetting front and resident time during quenching of a high temperature cylindrical brass block with water and emulsion jet at atmospheric pressure. The temperature is measured inside the block at a specific depth of 2mm from the hot surface. The movement of wetting front over the heated block surface is observed and the wetting delay between water and emulsion jet is compared by graphical analysis and visual observation.

2. Experimental setup and procedure

The experimental setup consists of four major parts: a structure to support the test block, a heater to heat the block, the liquid circulation system and the temperature measuring system. The other requirement was to make proper insulation to

avoid heat losses. Fig. 2 shows a schematic diagram of the experimental setup that was used during our experiment. The total setup consist of water tank, pump, pipe, reducer, valves, nozzle, cylindrical steel block, insulation, gasket, variac, thermocouple, digital panel meter etc.
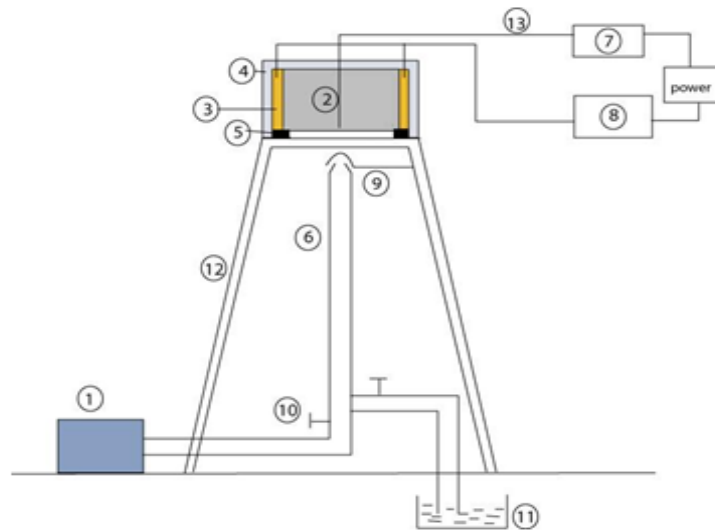
1. Pump, 2.Tested block, 3.Heater, 4.Insulation, 5.Gasket, 6.Nozzle, 7.temperature monitor, 8.Variac 9.Rotary shutter, 10.check valve, 11.Reservior, 12. Frame, 13.Thermocouple wire

Fig. 2. Schematic diagram of the experimental set up

The experiment is started with filling up the reservoir up to a certain level with the fluid. In case of cutting fluid the emulsion of water and oil was first made and then poured into the reservoir. Then the pump was switched on and a jet of fluid is initiated through a nozzle of 1 mm diameter, which is placed centrally 23 mm from the test surface. The different velocities were obtained by regulating the bypass gate valve. The jet velocity is then calculated by bucket and weight method. A shutter is mounted in front of the nozzle to prevent fluid from striking the block prematurely. The block is heated to the desired initial temperature by heating it with an electrical heater mounted around the block. After setting all initial conditions of the experiment, the shutter is opened for allowing the jet to strike at the center of the test surface of the heated block. The camera is employed to record flow pattern over the heated block surface.

The k type thermocouple measures the temperature inside the block and at the same time, time is recorded by a stop watch. The whole procedure is repeated for various jet velocity and initial block temperature. The experiment has been conducted under various test conditions for the purpose of clear understanding of the heat transfer characteristics during jet impingement quenching of hot brass block. The jet velocity and initial temperature of the brass block are varied.

Table 1. Test conditions of the experiment

Initial temperature of block, T_i (^{0}C)	Jet Diameter, d (mm)	Jet velocity, V (m/s)
250, 300, 350, 400, 450	1	3, 5, 10

3. Results and Discussion

Experimental resident time has been investigated as a function of test surface temperature for metal surfaces, two different liquid and three different jet velocities. A numerous number of graphs have been found for different conditions. In this study, the resident time has been estimated on the basis of two independent ways, one is from the temperature vs. time curve and the other is from the video images. In most of the cases both agreed well. Since video recording was not made for every case, only the first mean was sometimes employed to estimate the resident time. The pattern of the wave propagation is observed during the experiment closely. One of the most important objectives of the present study is to compare the wetting

delay and wetting front propagation of water and emulsion. The comparison is made by both graphical analysis and visual observation.

3.1. Comparison with graphical analysis

Graphical Analysis can be shown by Cooling curve i.e. Temperature vs. Time curve. Cooling curve for water represents ideal behavior and wetting delay can be observed in most of the cases. On the other hand, cooling curve for cutting fluid is nearly linear and it is difficult to obtain exact wetting delay from cooling curve. Wetting delay for most of the cases is found by visual observation.
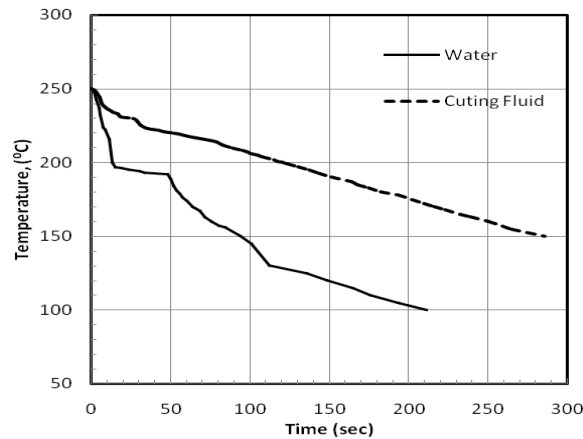

Fig. 3. Comparison of surface temperature and time curve at $T_i = 250\,^\circ C$, V= 5m/s

From the graph we can see that the resident time for cutting fluid is 26.13 seconds which is much less than the resident time of water which is 48seconds.We can also see the temperature at which the temperature remains quite constant is pretty high for cutting fluid as compared to water.

3.2. Comparison by visual observation

In addition to graphical analysis, Visual observation is a good indication of wetting delay. Since the specific heat of water is more than that of cutting fluid, wetting front for water propagate faster & wetting delay is less compared to cutting fluid. At $T_i = 350^\circ$ C, and V = 5m/s, Wetting delay for water & cutting fluid was found as 35 and 62 second respectively.
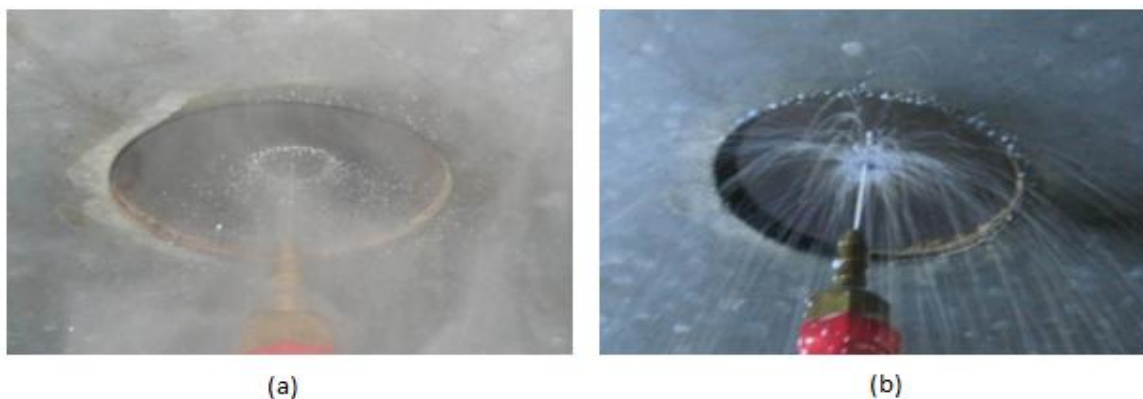

Fig. 4. Initial impact of jet at $T_i = 350^\circ$ C & V = 5 m/s (a) water; (b) cutting fluid

3.3. Effect of different parameters on wetting delay

The effect of different parameters on wetting delay plays an important role in analysis of quenching process. The most important parameters are the jet velocity and the initial block temperature. The wetting delay varies with these parameters through a direct relationship.

3.3.1. Effect of jet velocity

Generally the higher the velocity the the smaller should be the wetting delay. Because the higher velocity will remove the heat quickly from the heated surface . Therefore the wetting delay will be less. In this study we got these relationship between the jet velocity and wetting delay for most of the cases with pure water except some varaiations. But in case of emulsion as the temperature was decreasing linearly it was difficult to find out the wetting delay and therefore the direct relationship between the wetting delay and the jet velocity did not make out for most cases. In Fig. 5a for $T_i = 300^{\circ}C$, resident time in case of water for V = 3 m/s,5 m/s and 10 m/s has been plotted respectively. So from this figure it is evident that with the increase of velocity wetting delay decreases.
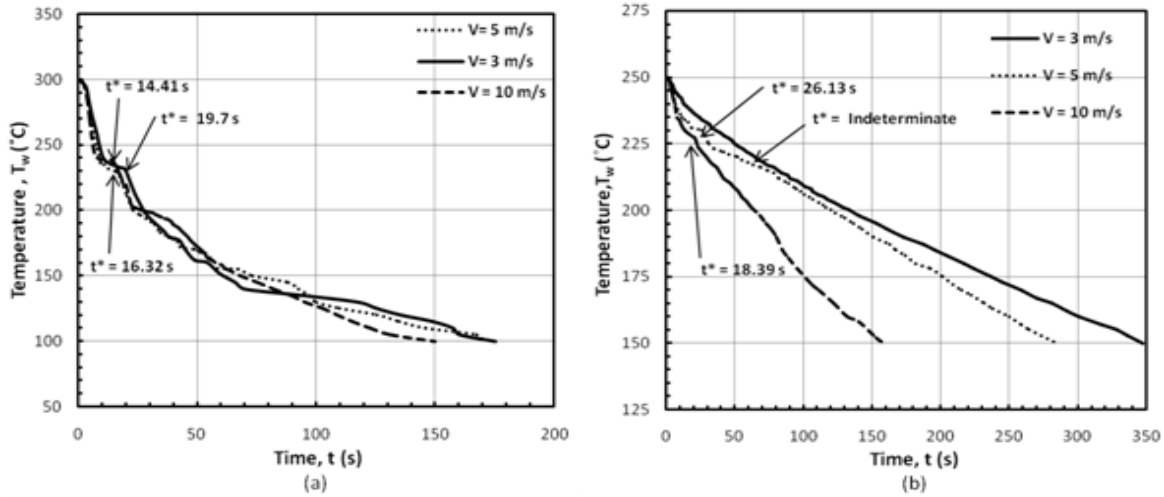

Fig. 5. Wetting delay for different water jet velocity (a) water at $T_i = 300^0C$; (b) cutting fluid at $T_i = 250^0C$

With cutting fluid we got similar result for initial temp. 250 $^{\circ}$C, 300 $^{\circ}$C,400 $^{\circ}$C and 450 $^{\circ}$C.But in these cases the wetting delay could not be determined for some velocities. Fig. 5b shows the variation in wetting delay at different jet velocities for $T_i = 250$ $^{\circ}$C. For this case we also get a good indication of the direct relation between wetting delay and jet velocity.Thus we can say that the wetting delay decreases with the increase of jet velocity.

3.3.2. Effect of initial block temperature

The initial temperature of the test block is also influencial in terms of wetting delay. Generally the highly heated block will take more time to become cool. So, the wetting delay should be higher. In our present study we got almost similar results for most of the cases. Although in some cases the wetting delay could not be exactly found. The wetting delay for different initial block temperature with different velocities have been plotted in this section for both water and cutting fluid . The wetting delay for water at different initial block temperatures for V= 3 m/s is shown in the Fig. 6a. From this figure we see that with the increase of initial block temperature, wetting delay increases except for 250 $^{\circ}$C.
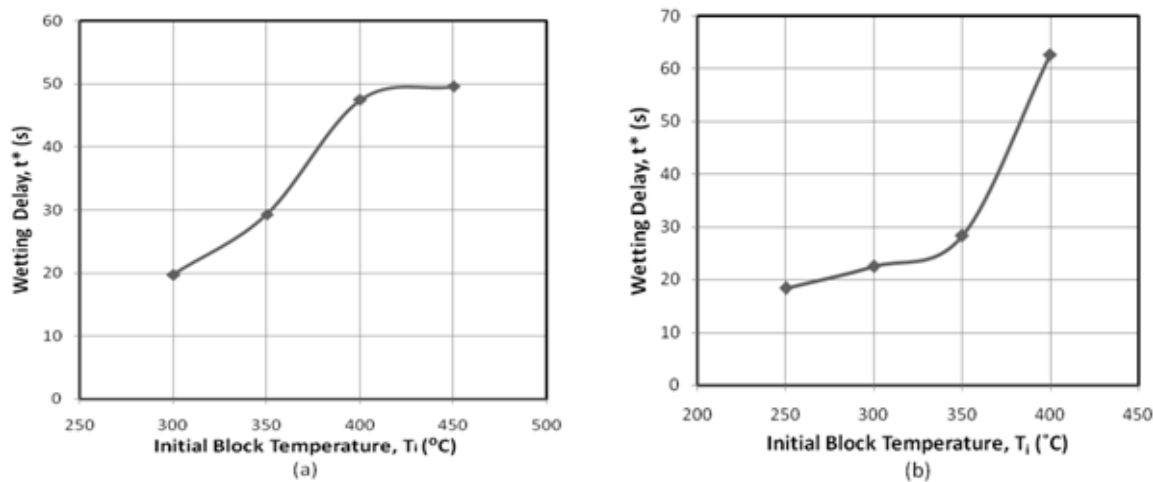

Fig. 6. Wetting delay at different initial block temperature (a) water at 3 m/s; (b) cutting fluid at 10 m/s

In case of cutting fluid the relationship between the wetting delay and the initial block temperature is not as clear as water. The wetting delay for cutting fluid at different initial block temperatures for V = 10 m/s also shows similar results as shown in Fig. 6b. Thus we can say that the relationship between wetting delay and initial block temperature was almost similar in all the cases except some variations.

4. Conclusions

The study has focused on the wetting delay parameter which is very important in investigating the underlying mechanisms of quenching process. Therefore, from the observations of the movement of wetting front and wetting delay the following conclusions can be drawn:

1. The wetting delay for brass block during jet impingement of water was very significant and easily identified in most of the cases. But in some cases we could not clearly identify the wetting delay.

2. The wetting delay during jet impingement of cutting fluid was not as clear as water though in some cases we got good indication of the wetting delay.

3. The wetting delay in case of cutting fluid is much higher than that of water. This is due to the fact that the cutting fluid we used is a 1:20 mixture of cutting oil (used in machine shop) and water. So the thermal conductivity of water was decreased as well as the heat removal rate.

4. In case of cutting fluid the wetting front took a long time to propagate and in some cases with lower velocities the whole surface could not be wetted by the jet. This is because the surface becomes oily just after the jet strikes the block which resist the front to propagate.

5. The resident time of wetting front increases with increasing initial temperature and with decreasing jet velocity. The higher velocity removes the heat quickly from the heated surface and therefore the wetting delay is less.

References

[1]   A. M. C. Chan and S. Banerjee, Refilling and Rewetting of a Hot Horizontal Tube, Part I: Experiments,   Trans. ASME, *Journal of Heat Transfer*, Vol. 103, pp. 281−286, 1981.
[2]   R. A. Nelson, Mechanism of Quenching Surfaces, in N. P. Cheremisinoff (ed.), Handbook of Heat and Mass Transfer, Vol. 1, Heat Transfer Operations, Gulf Publishing Co.,Houston, TX, pp. 1103−1153, 1986.
 [3]   B.D.G. Piggott, E.P. White, R.B. Duffy, Wetting delay due to film and transition boiling on hot surfaces, Nucl. Eng.Des. 36 (1976) 169–181.
[4]   Mozumder, A. K., "Thermal and Hydrodynamic Characteristics of Jet Impingement Quenching for High Temperature Surface", Ph.D thesis, Graduate School of Science and Engineering, Saga University, Japan, 2006.
[5]   Mozumder, A. K., Monde, M. and Woodfield, P. L., "Delay of wetting propagation during jet impingement quenching for a high temperature surface", Int. J. of Heat and Mass Transfer 48 pp. 2877-2888, 2005.
[6]   Mozumder, A. K., Monde, M. and Woodfield, P. L., and Islam, M. A., "Maximum heat flux in relation to quenching of a high temperature surface with liquid jet impingement", Int. J. of Heat and Mass Transfer 49 pp. 2877-2888, 2006.
[7]   D.E. Hall, F.P. Incropera, R. Viskanta, Jet impingement boiling from a circular free surface jet during quenching.Part 2. Two-phase jet, ASME J. Heat Transfer 123 (No. 4) (2001) 911–917.

5th BSME International Conference on Thermal Engineering

Probabilistic Structural and Thermal Analysis of a Gasketed Flange

Rama Subba Reddy Gorla

Department of Mechanical Engineering, Cleveland State University, Cleveland, Ohio 44115 USA

Abstract

Performance of a flange joint is characterized mainly by its 'strength' and 'sealing capability'. A number of analytical and experimental studies have been conducted to study these characteristics under internal pressure loading. However, with the advent of new technological trends for high temperature and pressure applications, an increased demand for analysis is recognized. The effect of steady-state thermal loading makes the problem more complex as it leads to combined application of internal pressure and temperature. Structural and thermal analysis of a gasketed flange was computationally simulated by a finite element method and probabilistically evaluated in view of the several uncertainties in the performance parameters. Cumulative distribution functions and sensitivity factors were computed for Stress Intensities and Von Mises Stresses due to the structural and thermodynamic random variables. These results can be used to quickly identify the most critical design variables in order to optimize the design and make it cost effective. The analysis leads to the selection of the appropriate measurements to be used in structural and heat transfer analysis and to the identification of both the most critical measurements and parameters. Conventional engineering design methods are generally deterministic. But in reality, many engineering systems are stochastic in nature where a probability assessment of the results becomes a necessity. This probabilistic engineering design analysis assumes probability distributions of design parameters, instead of mean values only. This enables the designer to design for a specific reliability and hence maximize safety and quality and cost. In the present work, thermal and structural analysis on the flange was performed to obtain the areas of maximum stress under the given boundary conditions. The product was modeled and then
Key words: Probabilistic analysis, finite element analysis, gasketed flange, thermal analysis

Keywords: Probabilistic analysis, finite element analysis, gasketed flange, thermal analysi

1. Introduction

Gasketed flange joints have been widely used in industry and have been the subject of detailed research for many centuries. The most significant contribution is by Waters et al. [1], for comprehensive flange design and became the basis of the well-known Taylor Forge method, which involves modeling of the joint elements using simplified plate and shell theory with known boundary conditions, and then combining the elements to derive stresses in various parts. Wide acceptance and the relative simplicity in its application has made the Taylor Forge method the most widely used flange design technique and is the basis of BS 5500 [2], ASME VIII [3] and many other codes. Murray and Stuart [4] performed flange analysis for taper hub flange, removing many of the assumptions of Water's model. A number of numerical studies are available for internal pressure loading only [5, 6]. Extensive experimental studies for combined internal pressure, axial and bending loading were performed by Abid et al. [7] to observe a joint's behavior.

To cost effectively accomplish the design task, we need to formally quantify the effect of uncertainties (variables) in the design. Probabilistic design is one effective method to formally quantify the effect of uncertainties. In the present study, a probabilistic analysis is presented for the influence of measurement accuracy on the random variables for Stress Intensities and Von Mises stresses from a Flange Assembly. Small perturbation approach is used for the finite element methods to compute the sensitivity of the response to small fluctuations of the random variables present. The result is a parametric representation of the response in terms of a set of random variables, which can be used to estimate the characteristics of the selected response variables such as stresses, heat transfer rate, pressure or temperature at a given point.

2. Model and the Approach

The flange assembly in question is a conventional gasketed flange attached to a pipe of the same material and bolted to the other mirrored flange with a gasket in between them. The material for the flange and the pipe is ASTM A105, the bolt is ASTM A193 and the gasket is ASTM A182. The bolt-up pressure is 254 MPa. This is a pre-load on the model. The flanges are free to move in either the axial or the radial direction. This provides flange rotation and the exact behavior of stress in the flange, bolt and gasket. Symmetry conditions are applied to the gasket lower portion, both sides of the gasket, bolt cross-sectional area, both sides of the flange ring and the attached pipe. Bolts are constrained in the radial and tangential directions. A nominal pre-load of about 35% (254 MPa) of the yield strength of the bolt (723 MPa) is chosen as per the achieved maximum strain in the bolt at the applied torque of 505 N m, Abid et al. [5,7,16]. The associated ASME code does not specify the magnitude of pre-load for the bolts, only a minimum seating stress that relates to the gasket style and composition. There is a heated fluid flowing inside the assembly with an internal pressure of 15.4 MPa. The temperature of the fluid is 100°C and the ambient temperature is 20°C. The internal heat transfer coefficient (h_i) is 150 W/m^{2}per°C while the outside heat transfer coefficient (h_∞) is 20 W/m^{2}per°C. The young's modulus, Poisson ratio and other structural and thermal properties are taken for the materials specified.

The objective of the present work is to analyze, test and verify the area of maximum stress concentration and deformation in the flange joint. The work was based on the information provided by Abid M, Nash DH [5]. Deterministic analysis was performed using Finite Element Analysis (FEA) using the software ALGOR to find the locations of stress concentration. The results obtained were verified with Abid M. [8] and were found to be matching. A probabilistic analysis was performed using the NESSUS analysis software [11] to find the structural reliability and critical design parameters.
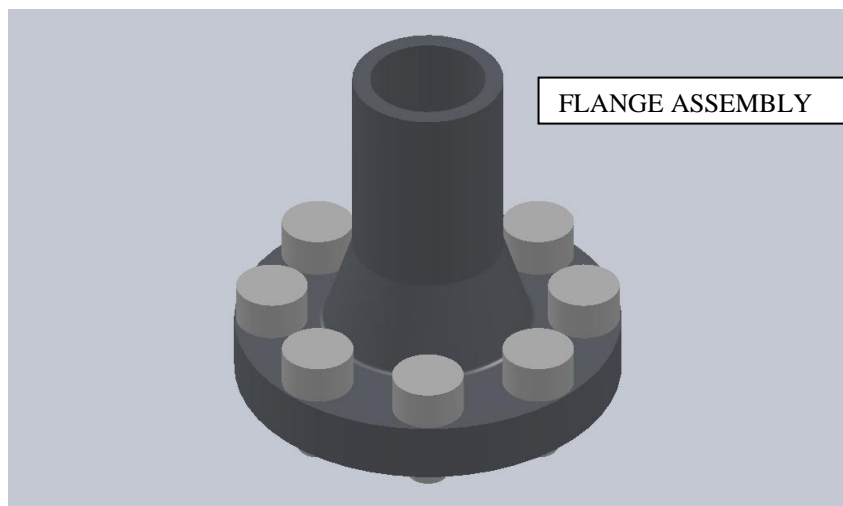

FLANGE ASSEMBLY

Figure 1: Solid Model of the Flange Assembly

We performed a mesh convergence study manually. The following basic steps were required:

- Create a mesh using the fewest, reasonable number of elements and analyze the model.
- Recreate the mesh with a denser element distribution, re-analyze it, and compare the results to those of the previous mesh.
- Keep increasing the mesh density and re-analyzing the model until the results converge satisfactorily.

This type of mesh convergence study enables to obtain an accurate solution with a mesh that is sufficiently dense and not overly demanding of computing resources. The model was analyzed with appropriate set of boundary conditions and material properties to find the temperature distribution. This is required to evaluate the thermal stresses in structural analysis.
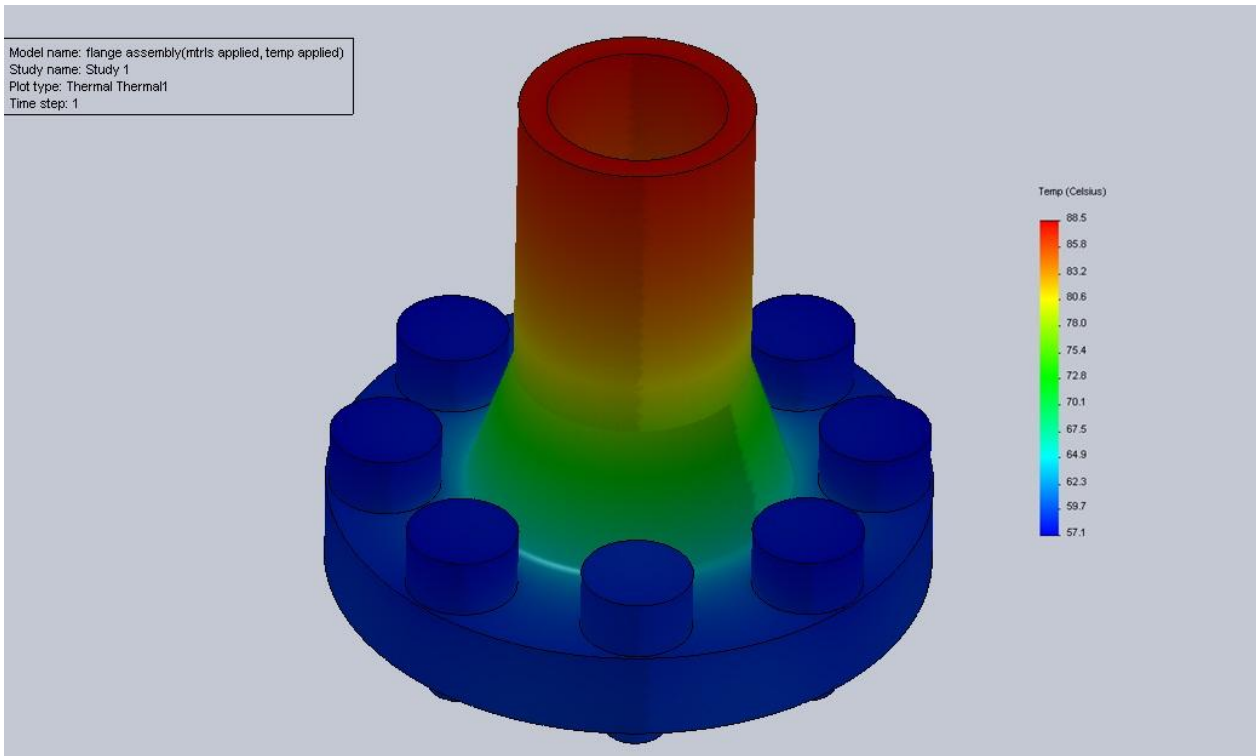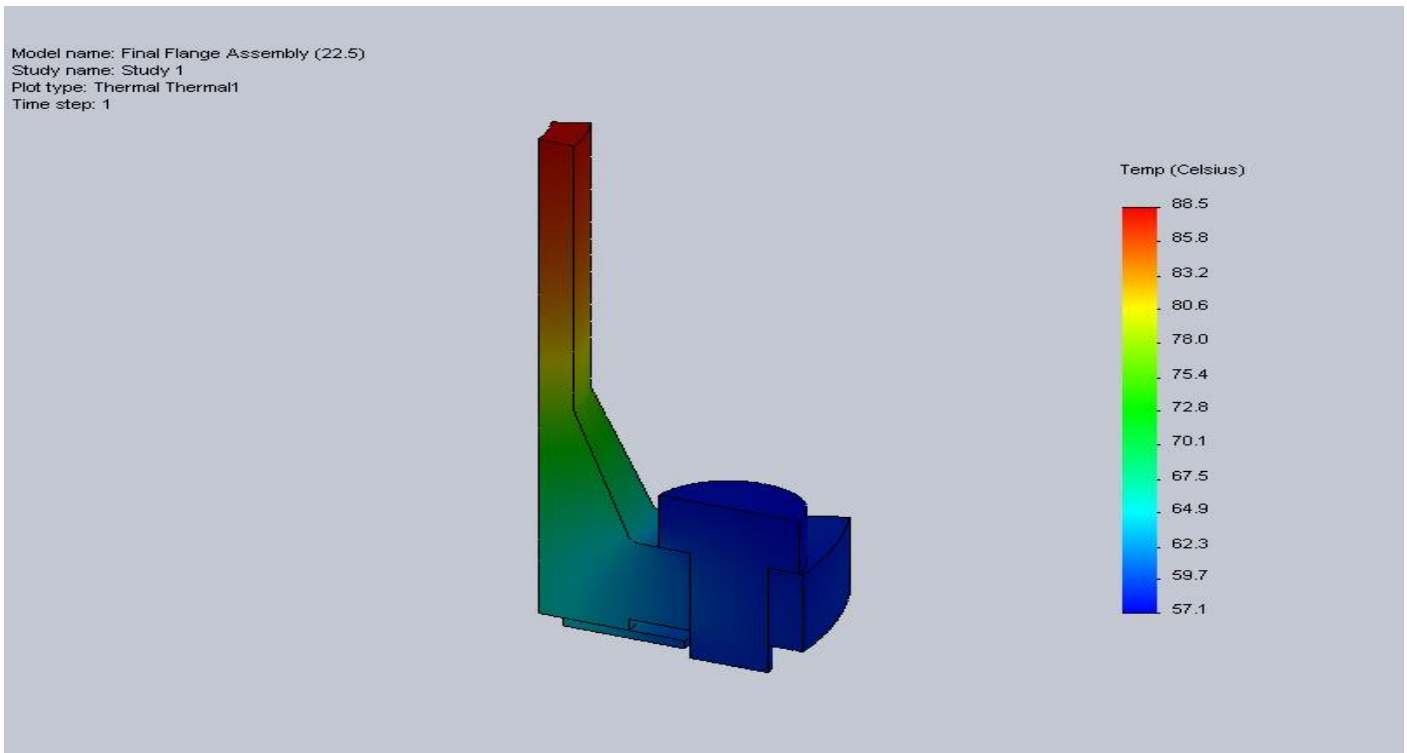
Figure 2 Temperature Distribution

Figure3: Sectional View of Von Mises Stress distribution

3. Results and Discussion

The temperature distribution is shown in Figure 2. The thermal stresses were analyzed from this temperature distribution (by linking it to the thermal analysis). Mechanical stresses were determined from the internal pressure and thermal effects. Maximum Von Mises Stress of 253.2 MPa and Maximum Stress Intensity of 282.4 MPa were found on the hub flange fillet and on the shoulder just below the flange-shoulder intersection.

The probabilistic analysis was carried out based on the first order reliability method (FORM). Forty random variables were used to compute maximum stresses on various probability levels for each of the two stresses viz. Von Mises Stress and Stress Intensity. Variation on Stresses due to the variation of each of the 40 random variables.

Cumulative distribution functions (CDF) and the sensitivity factors were developed by applying First order reliability method through NESSUS. Cumulative distribution functions for Maximum Von Mises Stress & Stress Intensity are shown in Figure 4. An important aspect of the FORM is the probabilistic sensitivity factors which help to identify the variables that contribute most of the reliability of the design. Probabilistic sensitivity factors include the sensitivity of p (Probability levels) with respect to a change in the mean value or the standard deviation of each random variable [11]. All random variables were assumed to be independent. A scatter of ±10% was specified for all the random variables. This variation amounted for two standard deviations. Normal distribution was assumed for all random variables. Maximum stress location was determined from a pre-analysis of the flange. This location was used to evaluate the cumulative distribution functions (CDF) and the sensitivity factors for stress response. The sensitivities for each of the Von Mises Stresses as a response are shown in the Figure 5. We observe that the overall model thickness, flange height, shoulder height, gasket inner diameter and bolt pressure have a huge influence on the maximum stresses followed closely by flange outside diameter, shoulder outside diameter, thermal conductivity, Poisson's ratio, tensile strength and yield strength.
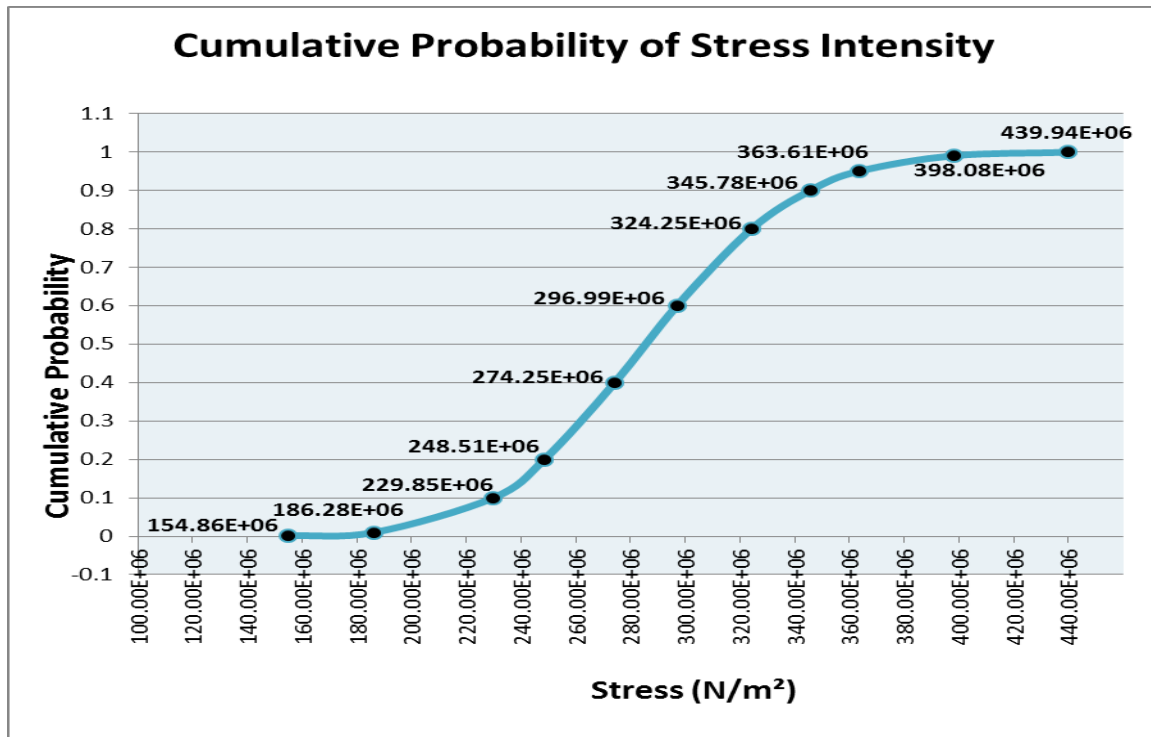

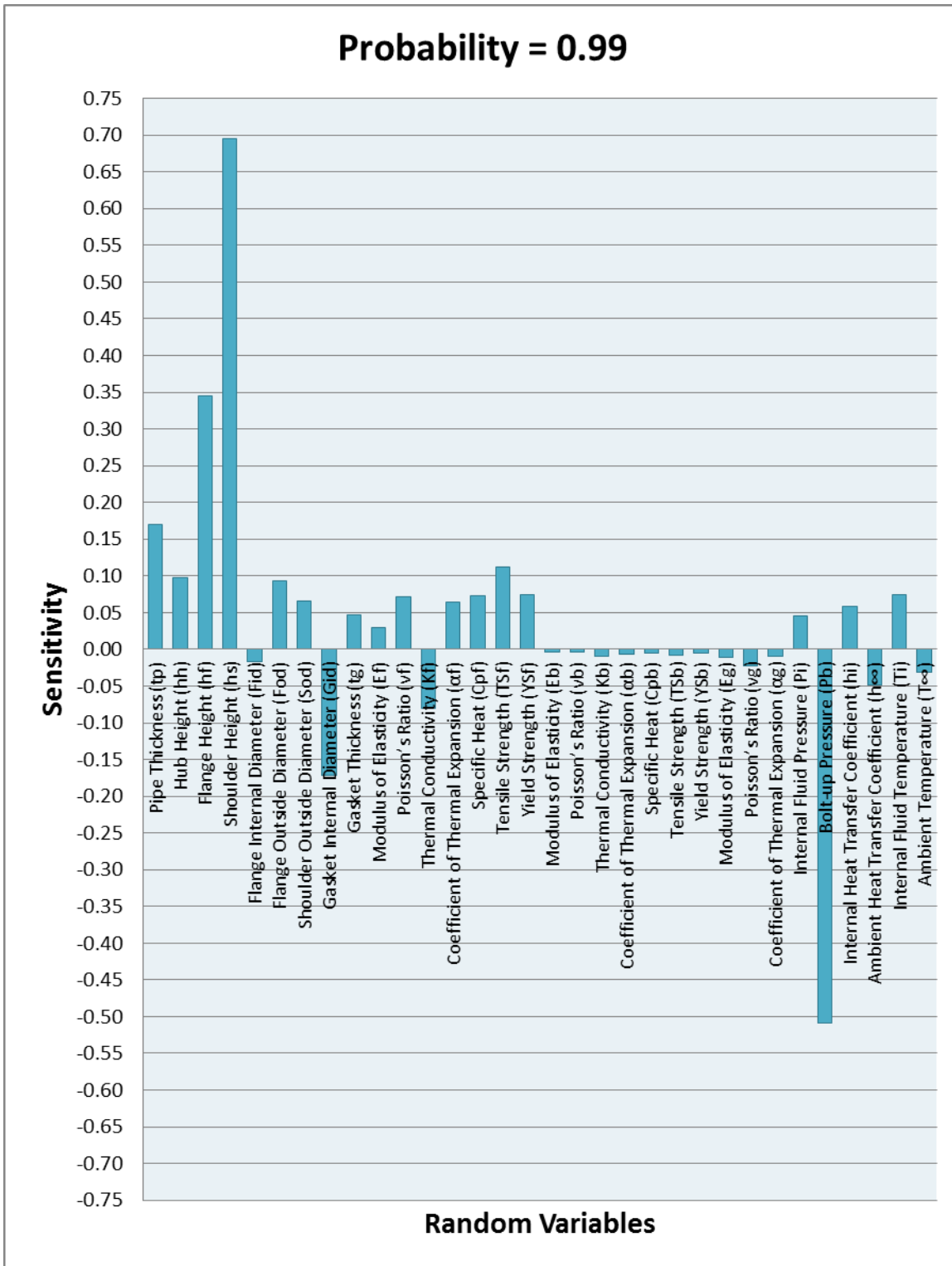Figure 4 Cumulative Probability Versus Stress

Figure 5: Sensitivity Factors for 0.999 Probability

4. Conclusions

Conventional engineering design methods are deterministic. The components of a machine are considered as ideal systems and parameter optimizations provide single point estimates of the system response. In reality, many engineering systems are stochastic where a probability assessment of the results is required. Probabilistic engineering design analysis assumes probability distributions of design parameters, instead of mean values only. This enables the designer to design for a specific reliability and hence maximize safety, quality and cost. The approaches for incorporating probabilistic effects in design include the use of factors of safety, the use of the worst case design and the use of probabilistic design. Utilizing the uncertainties in the estimations, deterministic engineering design uses factors of safety to assure that the nominal operational condition does not come too close to the point where the system will fail. The approximation of minimum properties and maximum loads known as the absolute worst case gives information about this critical point. This approach limits the optimization capability of a system and fails to provide important information about the system lifetime.

In this paper, deterministic method was supported by non-deterministic approach to find out the parameters responsible for the development of stresses. The novelty in this approach is the probabilistic evaluation of the finite element solution for the design problem. Cumulative distribution functions (CDF) and sensitivity factors were computed for Von Mises Stresses and Stress Intensities generated due to random variables in the design. Our goals were to first check for the area of maximum stresses and deformation and then carry out the probabilistic analysis to get a better picture of the effect of random variables on the stresses. Probabilistic analysis helps the designer to choose a suitable material/ geometry from the available set of parameters. The cumulative distribution functions (CDF) completely describes the probability distribution of a real-valued random variable. Sensitivity factors provide information about the relative importance of the variability or uncertainty of all of the input variables and their influence on the resulting fatigue life. These are the parameters the designer will be looking for designing an optimum reliability based design. Slight alteration of those will have a significant impact on the performance of the design in practical conditions.

5. References

[1] Waters EO, Wesstrom DB, Rossheim DB, Williams FSG. Formulas for stresses in bolted flanged connections. Trans ASME 1937;59:161-170.

[2] BS 5500. Unfired fusion welded pressure vessels. British Standards Institution, London, UK; 1991.

[3] ASME Boiler and Pressure Vessel Code, Section VIII. American Society of Mechanical Engineering, New York, USA; 1998.

[4] Murray NW, Stuart DG. Behaviour of large taper hub flanges. Proceedings of symposium pressure vessel research towards better design. Institute of Mechanical Engineers; 1961: p. 133.

[5] Abid M, Nash DH. Comparative study of the behaviour of conventional gasketed and compact non-gasketed flanged pipe joints under bolt up and operating conditions. Int J Pressure Vessels Piping 2004; 80:831–41

[6] Power DJ. A study of conventional and unconventional flanged pipe joint styles using non linear finite element analysis techniques. MPhil Thesis. University of Strathclyde, UK; 1997

[7] Abid M. Experimental and analytical studies of conventional (gasketed) and unconventional (non gasketed) flanged pipe joints (with special emphasis on the engineering of 'joint strength' and 'sealing'). PhD Thesis. University of Strathclyde, UK; 2000

[8] Kalbhor M. Structural and Thermal Analysis of Flange For LNG Applications. Master's Thesis. Cleveland State University, OH; 2009

[9] Abid M. Determination of safe operating conditions for gasketed flange joint under combined internal pressure and temperature: A finite element approach. Int J Pressure Vessels and Piping 2006; 83: 433–441

[10] Southwest Research Institute, " Probabilistic Structural Analysis (PSAM) for select Space Propulsion System components, " Final report NASA Contract NAS3-24389, NASA Lewis Research Center, Cleveland, Ohio, (1995).

[11] D.S Riha, B.H Thacker, H.R Millwater, Y.T Wu and M.P Enright, " Probabilistic Engineering Analysis using the NESSUS Software," Southwest Research Institute San Antonio, TX . AIAA-2000-1512.(2000)

5th BSME International Conference on Thermal Engineering

Investigation of Material Removal Characteristics in EDM of Nonconductive ZrO$_2$ Ceramic

Abdus Sabur,* Mohammad Yeakub Ali, Md. Abdul Maleque, Ahsan Ali Khan

Department of Manufacturing and Materials Engineering, Faculty of Engineering, International Islamic University Malaysia, P.O. Box No. 10 50728, Kuala Lumpur, Malaysia

Abstract

The use of nonconductive ceramic materials is increasing rapidly in industrial and engineering applications due to its high hardness, low thermal conductivity, and resistance to oxidation. Machining operations for fabricating structures from nonconductive ceramic materials are difficult and most of the traditional machining techniques are not applicable because of its high brittleness. Electro discharge machining (EDM) technique, a noncontact machining process, is applied for processing nonconductive ceramic ZrO$_2$ using assisting electrode. In this technique, pyrolytic carbon layer on the ceramic surface formed by the cracked carbon from the carbonic dielectric, plays the key role for continuous EDM. The formation of pyrolytic carbon and its stability depends upon the input power, workpiece material, tool electrode material, dielectric substance, polarity, and discharge duration. In this study, experiments were done to investigate the effect of input power on the material removal rate (MRR) and to explore the material removal mechanism. The experimental results show that the material is removed in EDM of nonconductive ZrO$_2$ ceramic mostly by spalling and it increases with the increase of input power.

Keywords: Nonconductive ceramic; Electro discharge machining; Assisting electrode; Pyrolytic carbon.

1. Introduction

Nonconductive ceramics are composed of metallic and non-metallic elements. The covalent and ionic bonds of elements make these ceramics much stronger than metals. Nonconductive ceramics are also known as engineering ceramics or advanced ceramic materials. Due to the excellent chemical and physical properties, nonconductive ceramics have been using for many years in automotive spark plugs as an electrical insulator and high temperature resistant. They are now used in multifarious fabrication of domestic, industrial, building products and art objects. Examples include cutting tools, self-lubricating bearings, turbine blades, internal combustion engines, heat exchangers, ballistic armour, ceramic composite automotive brakes, diesel particulate filters, a wide variety of prosthetic products, piezo-ceramic sensors [1]. Currently, micro-parts made of engineering ceramics are used in biomedical field to fabricate femoral heads and acetabular cups for total hip replacement, dental implants and restorations, bone fillers and scaffolds for tissue engineering. In near future, the need for tough, strong and stable bioinert ceramics should be met by either nano-structured Al$_2$O$_3$ and ZrO$_2$ based ceramics and composites or by non-oxide ceramics [2], [3]. Nonconductive ceramics cannot be machined by traditional metallic tools because of their high brittleness and hardness. Hence, nonconventional machining such as chemical machining, abrasive water jet machining, ultrasonic machining, laser beam machining, electro discharge machining are used in processing of

---

* Corresponding author. Tel.: +603-61964507; fax: +603-61964477.
E-mail address: asabur72@yahoo.com

structures from nonconductive ceramic materials [4]. EDM is a known process for producing structures from electrically conductive materials with high dimensional accuracy and good surface finish. Most of the engineering ceramics such as Al_2O_3, ZrO_2, Si_3N_4 and SiC are electrically nonconductive. Therefore, to apply EDM for structuring nonconductive ceramic materials, a basic technique is developed in which a conductive metallic layer is applied on the surface of the workpiece [5]. This additional conductive metallic layer is referred as assisting electrode (AE). The initial electrical sparks occur in the machining gap between the tool electrode and the assisting conductive electrode. In this method, kerosene is used as dielectric fluid. After the finishing of AE layer, carbon particles are cracked due to the disassociation of kerosene molecule at high instantaneous energy and create a layer of pyrolytic carbon on the machined surface of the electrically nonconductive ceramic. This carbonic layer provides the essential electrical conductivity to progress the process. Adhesive copper or aluminium foil, coating of graphite or carbon, silver varnish and copper, silver or gold sputtered on the workpiece surface can be used as AE [6], [7], [8]. Machining of Si_3N_4, SiC and ZrO_2 has been done successfully by EDM using assisting electrode and pyrolytic carbon technique. But in processing of Al_2O_3, the creation of conductive pyrolytic carbon layer at high temperature during EDM discharge is quite different compared to other engineering ceramics. The formation of pyrolytic carbon layer on the Al_2O_3 substrate depends upon the degree of purity of the material. In EDM of low purity and porous Al_2O_3, the pyrolytic layer can be created during the process. But it does not form on the surface of highly pure Al_2O_3 ceramic [9]. It is observed that the free energy of forming Al_4C_3 is rather high as compared to those of ZrC. As a result, creation of conductive pyrolytic carbon layer on Al_2O_3 is very difficult and machining becomes unstable [10]. Microstructures from insulating Si_3N_4 are successfully fabricated by EDM using AE method in which copper and carbon powder is mixed and applied on ceramic surface [11]. AE method also can be applied in electro discharge milling for nonconductive ceramics [1], [12]. In this process, a conductive metallic wheel is used as tool electrode mounted on a rotary spindle driven by an AC motor. The tool electrode and the assisting electrode are connected to the positive and negative poles of the pulse generator respectively. The insulating ceramic workpiece is mounted on a numerically controlled table. Thin conductive metallic sheet is supplied continuously on the workpiece. So, water also can be used as dielectric. Adhesive copper and aluminium foil are used in EDM of ZrO_2 to get the optimized machining parameters in certain machining conditions [13]. The microstructures of high aspect ratio from nonconductive ZrO_2 have been fabricated successful by micro-EDM with a special arrangement of tool electrode [6]. The effect of electrode material on EDM of Al_2O_3 is investigated using copper, graphite (Poco EDM-3) and copper-infiltrated-graphite (Poco EDM-C3) electrodes. The results show that Al_2O_3 cannot be machined with pure copper electrode with positive polarity. But graphite tool electrodes can be used with both the polarities. Positive tool polarity gives higher MRR and less electrode wear rate (EWR) [14]. In EDM of conductive materials, material is removed mostly by melting and evaporation, but the main material removal mechanism in EDM of nonconductive ceramics is spalling which occurs due to the alternating thermal load of the electrical sparks [6], [15], [16]. Thus material removal is influenced greatly by the input energy level [15], [17]. Several works have been done to investigate the effect of parameters such as voltage, current, discharge duration on MRR in EDM of nonconductive ceramics, but the effect of input power on MRR in EDM of nonconductive ceramics is not known. Precise removal of material (i.e. MRR) is essential to know to fabricate intricate and micro product. This paper aims to investigate the effect of input power on the continuous machining of nonconductive ceramics and investigate the spalling effect in EDM of ZrO_2 ceramic.

2. Experimental

The schematic diagram of the experimental setup of EDM for nonconductive ceramic with the AE is shown in Fig 1. The machining has been conducted using NC die-sinking EDM machine (EX22, Mitsubishi, Japan). In the present experiments, 92% pure ZrO_2 ceramic plate (20 mm x 15 mm x 10 mm) is used as workpiece. The properties of the workpiece material are listed in the Table 1. The copper tool electrode (3 mm x 3 mm) is used. The workpiece and the tool electrode were cleaned by acetone before machining. Since the workpiece is electrically nonconductive, its surface is covered by an adhesive copper layer to occur the sparks. After the removal of this external layer, a new conductive layer is created instantaneously on the machined surface using cracked carbon combined with the debris of tool electrode material. This layer acts further as an assisting electrode. Copper foil has excellent electrical conductivity and easy to remove after machining without any damage. After machining, the workpiece is cleaned again by acetone before weighing. Electronic balance (B204-S Mettler Toledo, Switzerland) is used to take the weight of workpiece before and after the machining. The important machining parameters used in the experiments are summarized in the Table 2. To investigate the effect of input power in EDM of nonconductive ceramics, experiments are done varying the input power keeping other parameters constant.

3. Results and discussions

The ZrO_2 ceramic workpiece machined by EDM is shown in Fig. 2 and SEM images of machined surface are shown in Fig. 3. Cavities of various depths such as 1 mm, 2 mm, and 4 mm are created on the ZrO_2 workpiece. The pyrolytic carbon layer on the machined surface is produced continuously using kerosene as dielectric fluid and adhesive copper foil as initial assisting electrode. The main material removal mechanism in EDM of nonconductive ceramic materials is spalling. However, a small fraction of ceramic materials can be removed by melting and vaporization [6]. In the SEM images, several cracks are observed and it clearly reveals that the most of the material is removed due to spalling. Spalling also depends on the input energy. A minimum input power is required to create the pyrolytic carbon layer on the ceramic surface. The present experiment shows that at lower input powers, EDM could not be progressed on ZrO_2. The minimum input power of 1.1 KVA could start the machining creating a thin layer of pyrolytic carbon with very low MRR. Stable machining is attained at 1.2 KVA and more materials are removed at increased input powers. The effect of input power on the MRR is shown in Fig. 4. It is evident that MRR increases with the increase of input power at initial stages. This trend remains same from the input power of 1.1 KVA until 1.3 KVA. From 1.3 to 1.4 KVA, it is increased at lower rate (curve is less stiff). However, more experiments are needed to confirm the trend.
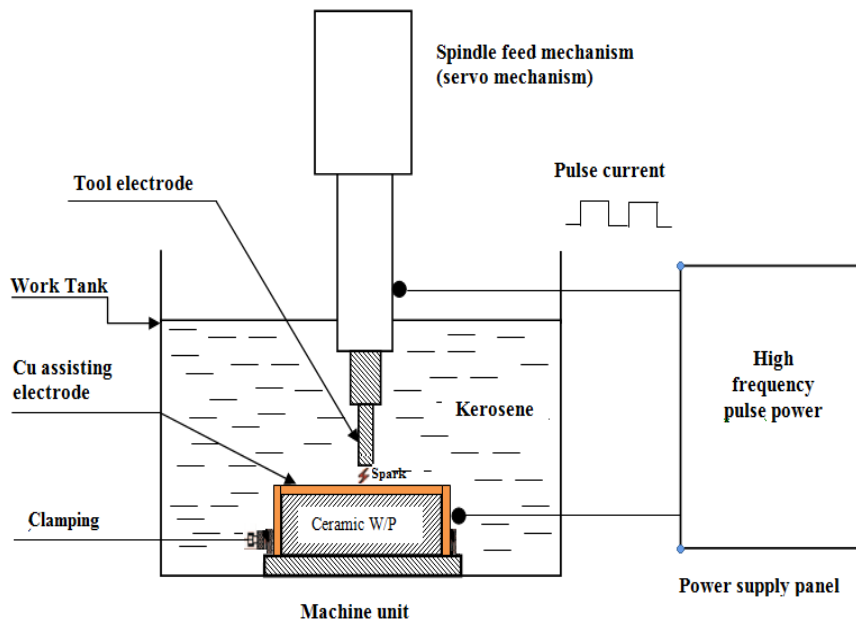

Fig. 1. Schematic diagram of the experimental setup

Table 1. Physical properties of workpiece material

Property	Value
Hardness (Hv)	1270
Melting temperature (^{0}C)	2720
Thermal conductivity (W/m K)	2
Specific heat capacity (J/g^{0}C)	0.4
Specific gravity (g/cm^3)	5.68
Electrical resistivity (Ω-cm)	1010

Table 2. The EDM conditions

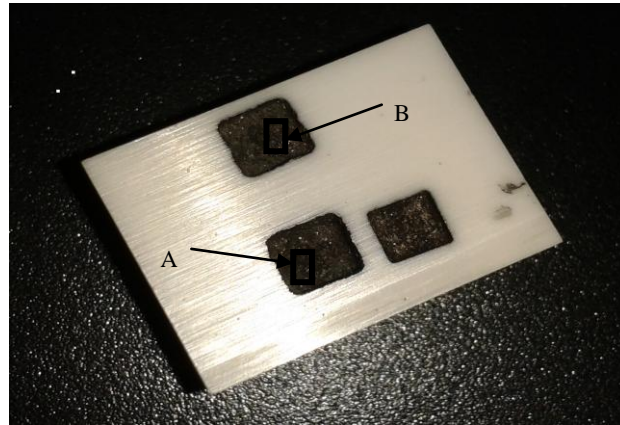| Working conditions	Description
Tool electrode	Cu
Tool polarity	-ve
Input power (KVA)	1.1, 1.2, 1.3, 1.4
Pulse-on-time, T_{on} (µs)	12
Pulse-off-time, T_{off} (µs)	12
Assisting electrode	Adhesive Cu foil
Dielectric fluid	Kerosene

Fig. 2. Three by three millimetres sized square cavities on ZrO_2 ceramic workpiece machined by EDM using adhesive copper foil as assisting electrode, copper tool electrode with –ve polarity at T_{on}=12 μs and T_{off} =12 μs . Input power A : 1.3 KVA, B : 1.4 KVA
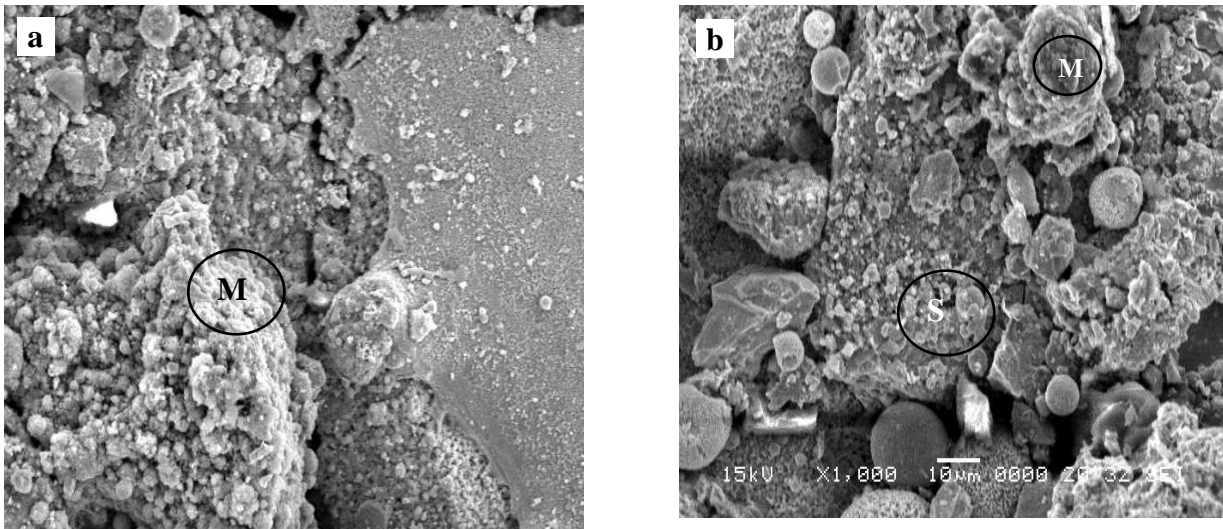

Fig. 3. Magnified SEM images of rectangular box of window A and B in EDMed ZrO_2 surface (a) window A in Fig. 2 (b) window B in Fig. 2 (M: melting, S : spalling)
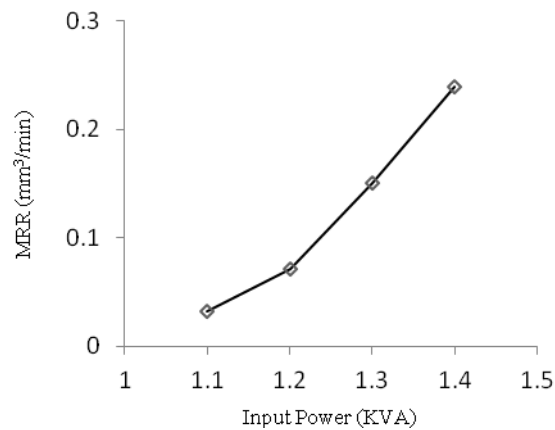

Fig. 4. The effect of IP on MRR in EDM of nonconductive ZrO_2 using adhesive copper foil as assisting electrode, copper tool electrode with –ve polarity at T_{on}=12 μs and T_{off} =12 μs

The reason can be explained by the Equation (1) [15].

$$F = \beta \sqrt{\frac{\rho E}{T_{on} T_{off} \, l}} \tag{1}$$

where, F is the maximum of the discharge force, β is the integral of C_p/C_v, ρ is the density of dielectric, E is the energy in the single pulse, T_{on} is the pulse-on-time, T_{off} is the pulse-off-time, l is the spark gap. It can be seen from "Equation (1)," the discharge force increases with an increase in the discharge energy. Thus, the amounts of workpiece material removed increase with an increase in the energy supplied. But it is observed that material removal is decreasing at higher energy level. In this stages, more power results rapid removal of base material with higher alternating thermal load. The pyrolytic carbon layer also is washed away rapidly from the machined surface before attaining desired thickness. Dielectric strength is very important in EDM of advanced ceramics. At higher input power, kerosene produces more free carbon particles and dielectric strength is reduced consequently. In this condition, rate of pyrolytic carbon formation is also reduced that may be another reason for decreasing MRR at higher input power in EDM of nonconductive ceramic materials.

4. Conclusions

Nonconductive ZrO_2 ceramic was machined by die-sinking EDM machine applying assisting electrode method. The effect of input power on material removal characteristics was investigated. Following conclusions can be drawn from the experimental observations and results.

1. Using adhesive copper foil as assisting electrode and copper tool electrode with –ve polarity in kerosene dielectric, EDM of nonconductive ZrO_2 ceramic is done effectively (Fig. 2).
2. In the EDM of nonconductive ZrO_2 ceramic, the material is removed mainly by spalling (Fig. 3a). A little amount of material is removed by melting and vaporization (Fig.3b).
3. The material removal can be increased by increasing the input power keeping other parameters constant (Fig.4).
4. After EDM, the external copper layer can be removed from the ceramic surface easily (Fig. 2).
5. Further experiments are needed to investigate the effect of higher IP on MRR.

Acknowledgements

References

[1]   Liu, Y. H., Ji, R. J., li, X. P., Yu, L. L., Zhang, H. F., Li, Q. Y., 2008. Effect of machining fluid on the process performance of electric discharge milling of insulating Al_2O_3 ceramic, International Journal of Machine Tools & Manufacture 48 (9), p. 1030.

[2]   Chevalier, J., Gremillard, L., 2009. Ceramics for medical applications: A picture for the next 20 years, Journal of the European Ceramic Society 29 (7), p. 1245.

[3]   Schubert, A., Zeidler, H., Wolf, N., Hackert, M., 2011. "Micro Electro Discharge Machining of Electrically Nonconductive Ceramics," AIP Conference Proceeding, 1353, p. 1303.

[4]   Ting, H. T., Abou-el-Hossein, K. A., Chua, H. B., 2009. Review of micromachining of ceramics by etching, Transactions of Nonferrous Metals Society of China 19 (Supplement 1), p. s1-s16.

[5]   Mohri, N., Fukuzawa, Y., Tani, T., Saito, N., Furutani, K., 1996. Assisting electrode method for machining insulating ceramics, CIRP Annals Manufacturing Technology 45(1), p. 201.

[6]   Hosel, T., Cvancara, T., Ganz,T., Muller, C., Reinecke, H., 2011. Characterization of high aspect ratio nonconductive ceramic microstructures made by spark erosion, Microsystem Technologies 17 (2), p. 313.

[7]   Hosel, T., Muller, C., Reinecke, H., 2011a. Spark erosive structuring of electrically nonconductive zirconia with an assisting electrode, CIRP Journal of Manufacturing Science and Technology 4(4), p. 357.

[8]   Schubert, A., Zeidler, H., 2009. "Machining of nonconductive ZrO2 ceramics with micro-EDM," Proceedings of 9th International Conference of the European Society for Precision Engineering & Nanotechnology, San Sebastian, Spain, 2, pp. 6-9.

[9]   Fukuzawa, Y., Mohri, N., Tani, T., Muttamara, A., 2004. Electrical discharge machining properties of noble crystals, Journal of Materials Processing Technology 149 (1-3), p. 393.

[10]   Mohri, N., Fukuzawa, Y., Tani, T., Sata, T., 2002. Some Considerations to Machining Characteristics of Insulating Ceramics-Towards Practical Use in Industry, CIRP Annals-Manufacturing Technology 51(1), p. 161.

[11]   Muttamara, A., Fukuzawa, Y., Mohri, N., Tani, T., 2003. Probability of precision micro-machining of insulating Si3N4 ceramics by EDM, Journal of Materials Processing Technology 140 (1), p. 243.

[12]   Liu, Y. H., Li, X. P., Ji, R. J., Yu, L. L., Zhang, H. F., Li, Q. Y., 2008. Effect of technological parameter on the process performance for electric discharge milling of insulating Al_2O_3 ceramic, Journal of Materials Processing Technology 208 (1-3), p. 245.

[13]   Chen, Y.F., Lin, Y.J. Lin, Y.C., Chen, S.L., Hsu, L.R., 2010. "Optimization of electrodischarge machining parameters on ZrO2 ceramic using the Taguchi method," Proceedings of the Institution of Mechanical Engineers, Part B: Journal of Engineering Manufacture 24(2), p. 195.

[14]   Muttamara, A., Fukuzawa, Y., Mohri, N., Tani, T., 2009. Effect of electrode material on electrical discharge machining of alumina, Journal of Materials Processing Technology 209(5), p. 2545.

[15]   Ji, R., Liu, Y., Zhang, Y., Wang, F., Chen, Z, Dong, X., 2011. Study on single discharge machining characteristics of non-conductive engineering ceramics in emulsion with high open voltage and large capacitor, Proceedings of the Institution of Mechanical Engineers, Part B: Journal of Engineering Manufacture DOI: 10.1177/0954405411404630.

[16]   Lauwers, B., Kruth, J. P., Liu, W., Eeraerts, W., Schacht, P., Bleys, P., 2004. Investigation of material removal mechanisms in EDM of composite ceramic materials, Journal of Materials Processing Technology 149 (1-3), p. 347.

[17]   Wong, Y.S., Rahmana, M., Lim, H.S., Han, H., Ravi, N., 2003. Investigation of micro-EDM material removal characteristics using single RC-pulse discharges, Journal of Materials Processing Technology 140, p.303.

5th BSME International Conference on Thermal Engineering

Effect of Annealing Temperature on Nanostructured WO$_3$ Films on p-Si Substrate

M.F. Hossain[a,*], and T. Takahashi[b]

aDepartment of Electrical & Electronic Engineering, Rajshahi University of Engineering & Technology, Rajshahi-6204, Bangladesh
bDepartment of Electrical and Electronic Engineering, University of Toyama, Toyama 930-8555, Japan
*Corresponding Author: faruk94_ruet@yahoo.com

Abstract

Nanostructured WO3 films are prepared on p-Si substrate by facing target sputtering (FTS) method with sputtering pressure, 0.1 Pa and 200W. The sample is annealed at 850°C in air with 5°C/min. The as-deposited and annealed WO3 films have been characterized by the Grazing incidence X-ray diffractometer, Field emission electron microscopy, and Ultraviolet-visible spectrophotometer. The surface morphology of the WO3 films strongly depends on the annealing temperature. An average diameter of the WO3 nanorod is 5-6 μm long and 800 nm diameter. It is revealed from optical study that the band-gap energy of WO3 films is around 2.85 eV. The surface morphology of nanostructured WO3 films has been discussed with the increase of annealing temperature.

Nomenclature

D	Crystallite size (nm)
A	Edge width parameter

Greek symbols

λ	Wavelength (nm)
θ	Diffraction angle (Deg.)
β	Full Width Half Maxima (FWHM)
α	Absorption coefficient (a. u.)
$h\nu$	Photon energy (eV)

---

1. Introduction

Hierarchical self-assembly of nanosized building blocks, including nanowires, nanobelts, nanoplatelets, nanotubes, etc. is an important process for the fabrication of functional electronic and photonic Nanodevices[1]. In this regard, remarkable progress has been made for the synthesis of complex inorganic materials with controlled architectures, sizes, morphologies, and patterns since these parameters represent key elements that determine their electrical and optical properties [2]. Among transition metal oxides, tungsten trioxide (WO$_3$) is of great interest and has been investigated extensively due to its many interesting structural and defect properties. Numerous applications of WO$_3$ optical and electronic based devices include electrochromic (EC) smart windows, flat panel displays, tunable EC photonic crystals [3], gas sensors[4, 5], water splitters, dye sensitized solar cells and batteries. For the fabrication of many of such devices and increasing their efficiencies,

nanostructured WO$_3$ films are required to be "thick and porous" enough to provide sufficient volume for producing high interaction areas. Besides, synthesis and assembly of "specific crystallographic phase" can further improve the characteristics of WO$_3$. Tungsten oxide (WO$_3$) is an *n*-type semiconductor and has been investigated extensively owing to their promising physical and chemical properties [6]. WO$_3$ shows good optical properties and proper chemical stability; that is, *Eg* in the range of 2.5–2.8 eV (λ of 400–450 nm) is very suitable for the energy region of visible light [7, 8]. The synthesis of one-dimensional (1D) nanostructures and the assembly of these nano meter-scale building blocks to form ordered superstructures or complex functional architectures offer great opportunities for exploring their novel properties and for the fabrication of nanodevices [9]. Thus for several techniques for the preparation of 1D tungsten oxide nanostructured films have been developed [6].

The deposition of WO$_3$ nanostructured films by facing targets sputtering technique is the newest fabrication method of thin films, with lower particle bombardment compared with the RF sputtering and DC sputtering, because of its special target arrangement. The FTS apparatus are very effective systems for depositing high quality thin films because plasma perfectly confines by the magnetic field between two targets. The thin films can be deposited in non-bombardment by electron ("damage free") conditions [10-12].

In this work, nanostructured WO$_3$ films have been deposited on Si-based substrate by using FTS method with sputtering pressure of 0.1 Pa and annealed at 850°C. The structural, surface morphological properties of nanostructured WO$_3$ films have been investigated and discussed.
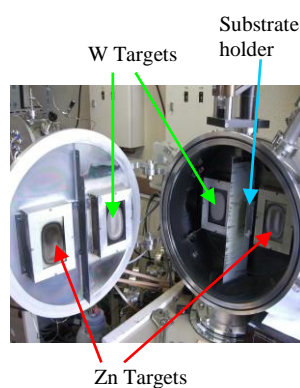

Fig. 1. Facing Target Sputtering system in our laboratory.

2. Experimental section

The FTS systems in our laboratory for preparing WO$_3$ thin layer is shown in Fig. 1[13]. The distance between the target-to-target, and the center of the targets' to the substrate were 100 mm and 50 mm, respectively. W rectangular plates (having 115 x 75 mm, thickness of 3 mm and purity of 99.95 %) were used as targets. The chamber was evacuated to a vacuum level of 7×10^{-4} Pa. The WO$_3$ nanoparticles were deposited reactively on Si-based substrate for 2hrs at DC input power of 200 W with sputtering pressure of 0.1 Pa and a fixed Ar to O$_2$ gas ratio (G$_R$) of 6:4 [14]. As-deposited WO$_3$ nanoparticles are annealing in a muffle furnace (TMF5, Thomas) under oxygen environment at 850°C for 2hrs, because as-deposited films are the amorphous structure. The thickness (2 μm) of the WO$_3$ films was determined with a mechanical surface roughness meter (SURFCOM Accretech, 1500 DX) using the step between film and substrate. The crystal structures of the TiO$_2$ films were determined by grazing incident X-ray diffraction (GIXRD) spectra (SHIMADZU XRD-6000) with Cu-Kα line. The data were recorded from 2θ values 20° to 80° with a step of 0.02. For GIXRD measurement incident angle was fixed at 0.45°. The optical properties of the films (prepared on glass substrate) were measured with JASCO V-550 spectrophotometer at room temperature within the wave length range 300-900 nm. The surface morphologies were studied using field emission scanning electron microscope (FE-SEM) with *Model:* JEOL, FE-SEM 6700F.

3. Results and discussions

Figure 2 shows the GIXRD patterns of as-deposited and annealed WO$_3$ thin film prepared on Si-based substrate. The GIXRD patterns of the as-deposited WO$_3$ films are found to be amorphous in nature, but crystalline films were obtained

when the film is annealed at high temperatures of 850 °C. The lines located at 23.12°, 23.6°, 24.28°, 28.80°, 47.24°, and 50.52° are assigned to the lattice plane reflection of triclinic WO_3 phase with lattice parameters a =0.7311 nm, b=0.7515 nm, and c=0.7679 nm (PC-PDF No. 83-0948). However, triclinic and monoclinic diffraction peaks almost overlap for many 2θ values and it is difficult to discriminate between these two phases. On the other hand, according to the phase diagram, the monoclinic and triclinic structures are the most common and coexist in WO_3 at temperatures higher than 500 °C [15]. The crystallite size of the particles has been estimated from the Debye–Scherrer's equation using the GIXRD line broadening as follows [16]: $D = 0.94\lambda / \beta\cos\theta$, where D is the crystallite size, λ is the wavelength of the X-ray radiation (Cu Kα=0.15406 nm), θ is the diffraction angle and β is the FWHM. A finite diffraction peak has been chosen for calculation of crystallite size. The diffraction peak (002) has been chosen for calculation. The derived grain size is 12.3 nm for the annealed WO_3 thin films.
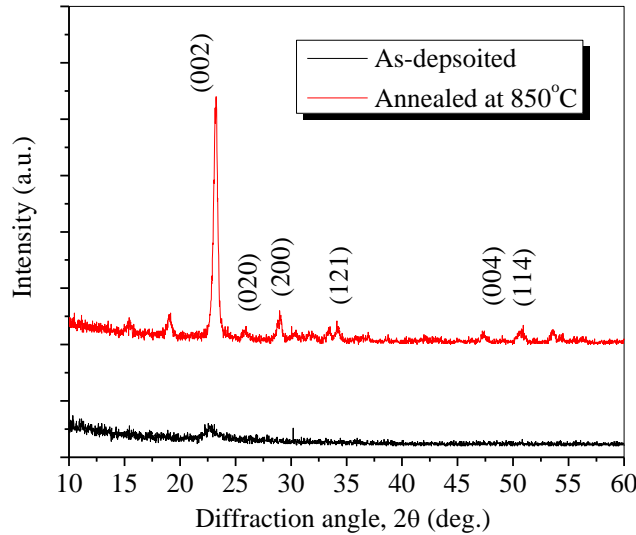

Fig.2. The GIXRD patterns of as-deposited and annealed WO_3 thin films
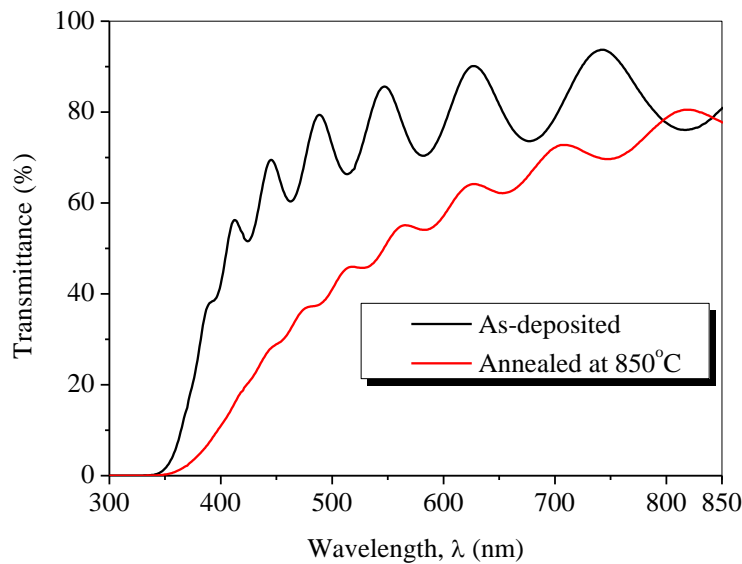

Fig.3. The optical transmittance spectra of as-deposited and annealed WO_3 thin films.

Figure 3 shows the transmittance spectra as a function of wavelength (300 - 800 nm) for as-deposited and oxygen-annealed WO_3 thin films, prepared in same conditions. The spectra of as-deposited WO_3 films show the usual interference pattern in the range of low absorption with a sharp fall of transmittance at the band edge. The oxygen-annealed WO_3 thin film is

yellowish in color. The oxygen-annealed WO_3 films have less interference. It has been observed that the transmittance edge shows the red-shift with the oxygen-annealed WO_3 films. It is may be due to the high crystallinity, observed within the sample of investigation. The average transmittance in region varies from 78% to 60.5% with as-deposited and annealed WO_3 films, respectively.

We assume an indirect transition between the top of the valence band and the bottom of the conduction band in order to estimate the optical band gap (Eg) of the films using the relation [18]: $\alpha(hv) \propto A(hv–E_g)^2$, where, α is absorption coefficient, A is the edge width parameter and hv is the photon energy. Figure 3 shows the plots of $(\alpha hv)^{1/2}$ versus the photon energy of the films grown at different sputtering powers. The optical band gap of the films was determined from the extrapolation of the linear plots of $(\alpha hv)^{1/2}$ versus hv at $\alpha=0$. The optical band gap of the films is 3.04 and 2.85 eV for as-deposited and annealed WO_3 films, respectively.
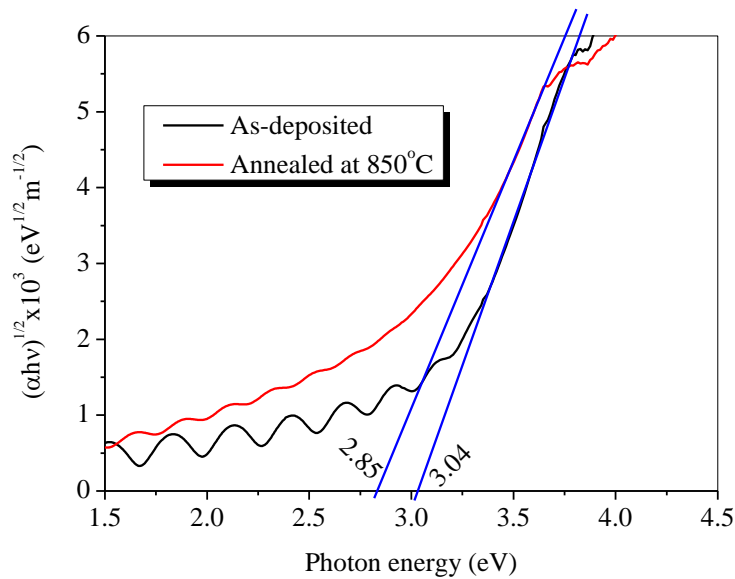

Fig.4. $(\alpha hv)^{1/2}$ versus energy for as-deposited and annealed WO_3 thin films.
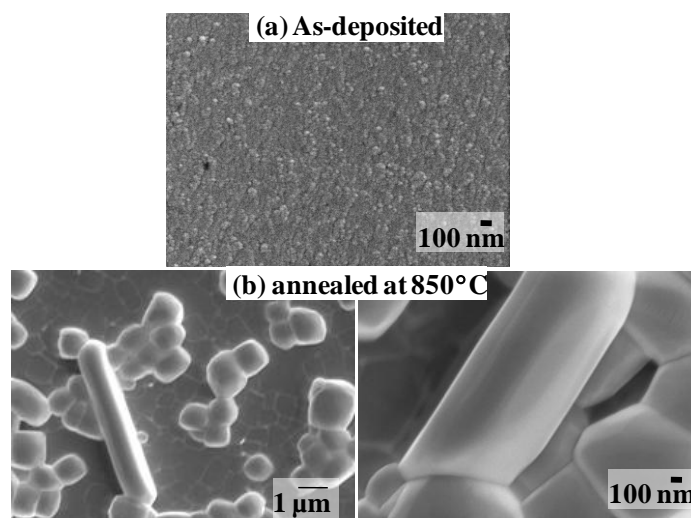

Fig. 5. FE-SEM images of as-deposited and annealed WO_3 thin films.

Figure 5 shows the surface structure and morphology of as-deposited and oxygen-annealed WO_3 films. From the Fig. 5(a), the as-deposited films have a smooth surface and nanograins are observed in a larger magnification, which reaffirms their

amorphous nature. The average-size of the nanograins is 13-17 nm. Oxygen-annealing of the films at 450 °C not only manifests in enhancement of particle size but also in a considerably different surface morphology. It is cleared from the Fig. 5(b) that the whole surface of this film is covered by nanorods and rectangular nanostructures. The average-size of each nanorod is approximately 5-6 µm long and 800 nm diameter. The rectangular shape has cross-section of ~750x~750 nm.

4. Conclusion

The nanostructured WO_3 films were successfully deposited on Si-based substrate by FTS method with sputtering pressure of 0.1 Pa and annealed at 850°C. High crystalline film is achieved with annealed at high temperature. The whole surface is covered with nanorods and rectangual nanostructures. As-deposited WO_3 films have amorphous structure. For the annealed WO_3 films, the average-size of each nanorod is approximately 5-6 µm long and 800 nm diameter. The rectangular shape has cross-section of ~750x~750 nm. This nanostructured WO_3 films can be used for photocatalytic, electrochromic and solar cells applications. The efficiency of these devices may be enhanced by increasing the thickness of WO_3 films.

Acknowledgement

References
[1] Li, S. Z., Zhang, H., Wu, J. B., Ma, X. Y., Yang, D. R., 2006, Crystal Growth Des. 6, p. 351.
[2] Zhang, H., Yang, D. R., Li, D. S., Ma, X. Y., Li, S. Z., Que, D. L., 2005, Crystal Growth Des. 5, p. 547.
[3] Boulmani, R., Bendahan, M., Lambert-Mauriat, C., Gillet, M., Aguir, K., 2007, Correlation between rf-sputtering parameters and WO_3 sensor response towards ozone, Sensors and Actuators B, 125, p. 622.
[4] Stankova, M., Vilanova, X., Llobet, E., Calderer, J., Bittencourt, C., Pireaux, J.J., Correig, X., 2005, Influence of the annealing and operating temperatures on the gassensing properties of rf sputtered WO_3 thin-film sensors, Sensors and Actuators B, 105, p. 271.
[5] Jimenez, I., Arbiol, J., Dezanneau, G., Cornet, A., Morant, J. R., 2003, Crystalline structure, defects and gas sensor response to NO_2 and H_2S of tungsten trioxide nanopowders, Sensors and Actuators B, 93, p. 475.
[6] Li, Y. B., Bando, Y.S., Golberg, D., 2003, Advanced Materials, 15, p. 1294.
[7] Nenadovich, M. T., Rajh, T., Micic, O. I., Nozik, A. J., 1984, Journal of Physics and Chemistry, 88, p. 5827.
[8] Maruska, H. P., Ghosh, A. K.,1978, Solar Energy, 20, p. 445.
[9] Gao, P.X., Wang, Z.L., 2002, Journal of Physics and Chemistry B., 106, p. 126533.
[10] Noda, K.., Kawanabe, T., Naoe. M., 1999, Journal of Magnetics and Magnetic Materrials 193, p. 71.
[11] Nose, M., Nagae, T., Yokota, M., Saji S., 1999, Surface and Coating Technology 116–119, p. 296.
[12] Kim, K.H., Son, I.H., Song K.B., 2001, Applied Surface Science 169–170, p. 410–414, 2001.
[13] Hossain, M.F., Takahashi, T., Ahmed, T., 2011, International Conference on Mechanical Engineering and Renewable Energy, Bangladesh.
[14] Hossain, M.F., Takahashi, T., 2010, Materials Chemistry and Physics 124, p. 940.
[15] Bittencourt, R., Landers, E., Llobet, G., Molas, X., Correig, M. A. P., Silva, J. E., Sueiras, Calderer, J., 2002, Journal Electrochemical Society 149, p. H8.
[16] Cullity, B.D., 1978, Elements of X-ray Diffraction, Addison-Wesley, Reading, MA, USA.

5th BSME International Conference on Thermal Engineering

Evaluation of Start of Crack Growth of Nuclear Material (SUS316NG) using Ultrasonic

Islam Md. NURUL[a], Yoshio ARAI[b] and Wakako ARAKI[c]

[a]Assistant professor, Department of Mechanical Engineering, Rajshahi University of Engineering and Technology,6204, Bangladesh.
[b,c]Professor, Department of Mechanical Engineering, Saitama University,338-8570, Japan.

Abstract

The detection of small fatigue cracks is of particular interest because it is a key element of remaining life prediction. In the present study low cycle fatigue crack initiation in austenitic stainless steel (SUS316NG) subjected to plane bending is observed and compared the change of back-reflection intensity of ultrasonic wave using the scanning acoustic microscope. Ultrasonic data is recorded as a function of the number of cycles and compared with slip band length measured optically. Surface observation using optical and scanning acoustic microscopy revealed that with increasing the number of fatigue cycle the slip band density increased and the amplitude of back reflection intensity gradually decreased before the slip band length increases. Due to the cyclic loading, dislocation density along persistent slip bands increase. The attenuation of ultrasonic back reflection intensity is due to the dislocation damping and this mechanism was considered.

Keywords: Back reflection intensity, scanning acoustic microscope, austenitic stainless steel, Low cycle fatigue, Crack growth

Nomenclature

A_{max}	maximum ultrasonic back reflection intensity
A_0	reference value of ultrasonic back reflection intensity
D_{psb}	damage evolution in persistent slip band
E	elastic modulus
H	radius of crystal grain
L	dislocation loop length
N	current number of fatigue cycle
N_f	number of cycle to failure
f	frequency of ultrasonic wave
α	attenuation
ν	poison's ratio
σ	stress
ε_p	plastic strain amplitude
Λ_0	initial dislocation density
Λ_{av}	average dislocation density
Λ_{psb}	movable dislocation density in persistent slip band

* Corresponding author. Tel.: +88-0721-750319; fax: +88-0721-750319.

* *E-mail address:* nurul93213@yahoo.com

1. Introduction

It is well known that low cycle fatigue crack initiation process are often associated with slip band which emergence at the free surface of metal and metallic alloys components subjected to cyclic loading [1,2]. The transgranular crack initiation process is a damage mechanism, also intergarnular cracking may occur in polycrystalline materials for high plastic strain amplitude [3,4]. Cyclic plastic strain plays an important role during cyclic loading for the change of internal structure of material. High plastic amplitude results surface relief generation, irreversible change in structure and fatigue crack growth starts. Surface relief observation on polished surface gives the information of fatigue crack initiation as well as their growth using high resolution method [5-8]. Due to easy and simplified instrumentation of ultrasonic method, it is used extensively as a technique of progressive change detection of material properties. At the very beginning of cyclic loading, the coefficient of attenuation increases linearly at slow rate but around 70-80% fatigue life, it increases rapidly [9-12]. It also has been reported that the high sensitivity and contactless aspects, electromagnetic acoustic transducer enabled to continuous measurement of the resonance frequency and attenuation co-efficient during the fatigue process using the polycrystalline copper[13]. In these studies, measurements of average volume in field were done using low frequency transducer. In this research, we measured the change of back-reflection intensity at the location where low cycle fatigue crack growth start in stainless steel using the scanning acoustic microscope and corresponding surface observation by optical microscope and proposed a method for evaluating remaining life of crack growth starts.

2. Materials and Methods

The material used in this experiment is a austenite stainless steel (JIS-SUS316NG) [14]. Chemical compositions and mechanical properties of tested material are given in Table 1 and Table 2 respectively. Fig. 1 shows the specimen shape and dimensions. The center portion of the test piece was polished using a series of emery paper (1200, 1500, 2000 and 3000 grades) and finally buffing was done using 0.3μm and 0.1μm alumina powder in order to identify the slip bands that are generated during the cyclic loading. Etching was done by using the solution of 40% water and 60% nitric acid to reveal the microstructure after the crack growth starts. The microstructure is shown in Fig. 2. The measured average grain diameter is 100μm.

Table 1 Chemical composition [wt.%]

Cr	Ni	C	N	Mn	Si	S	P	Mo	Cu	B	Co	As	Fe
17.4	11.9	0.02	0.07	1.69	0.31	0.002	0.023	2.25	0.11	0.009	0.19	0.004	Bal

Table 2 Mechanical Properties

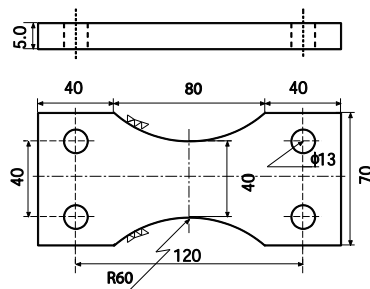| E (GPa)	ν	$\sigma_{0.2}$ (MPa)	σ_B (MPa)
190	0.25	261	583

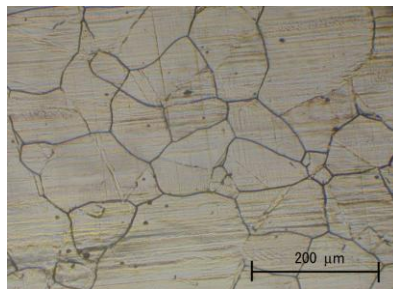Fig. 1. Specimen configuration [unit: mm]

Fig. 2. Micro-structure of test specimen

Strain controlled fatigue testing was performed on an electro-hydraulic material testing machine (MTS810). The loading was plane bending. The strain ratio was -1, loading frequency was 1 Hz and environment was the atmospheric. After applying the prescribed fatigue cycle, slip bands generation were observed using the optical microscope. The outline of ultrasonic apparatus is shown in Fig.3.
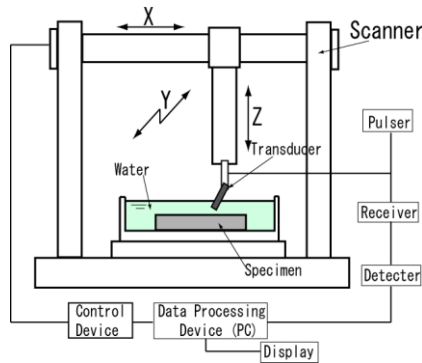

Fig. 3. Ultrasonic apparatus

Ultrasonic waves generated from the transducer transmitted to the specimen surface through water. The incidence angle is 30^0 which is larger than the critical angle, results in generation of surface waves. The surface waves were reflected by the grain boundaries. The leaky reflected surface wave was received at the incidence point by the same transducer. Fig. 4 shows ultrasonic wave propagation path. The central frequency of the transducer is 100 MHz, focal length is 12.5 mm in water and scan pitch is 5μm.
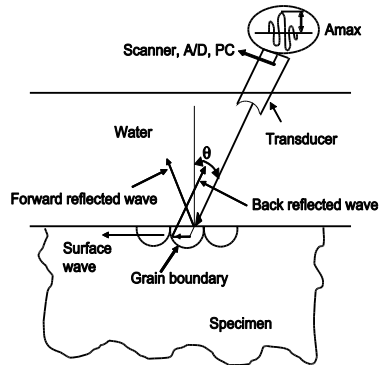

Fig. 4. Propagation path of the ultrasonic wave

3. Experimental Results

Fig. 5 shows the effect of plastic strain on the change of intergranular and transgranular crack growth and the density of slip lines. It is found that change of transgranular crack growth to intergranular crack growth increased with increasing the plastic strain amplitude and correspondingly intergranular crack growth to transgranular crack growth   was decreased. This figure also shows the increase in density of slip line with increase in plastic strain. Fig. 6 shows the ultrasonic microscope image   at crack initiated location from where we can detect and predict the start of crack growth simultaneously.
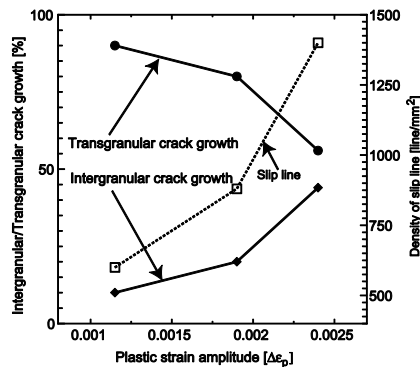

Fig.5 Relationship between nature of crack growth and density of slip line to plastic strain amplitude

In the ultrasonic microscope image, the inhomogeneous brightness distribution denotes the back reflection intensity from grain boundaries. The rectangular mark indicates the location from where we can predict the start of crack growth by ultrasonic decrease and on the circular mark indicates the location from where we can detect only. The brightness of the ultrasonic image in the rectangle   marked location, from N = 1 - 5000 cycles is decreased due to fatigue damage accumulation and then starts to increase at N= 5300 cycles and circle marked location brightness increased without tart to decrease. Fig. 7 shows the optical microscope observations on corresponding number of cycles of ultrasonic microscope image at same location (rectangular mark) and found that before increasing the brightness, the length of black line (indicated by arrow mark) remains unchanged but when the brightness start to increase   correspondingly the length of the black line start to increase which indicate the start of crack growth.
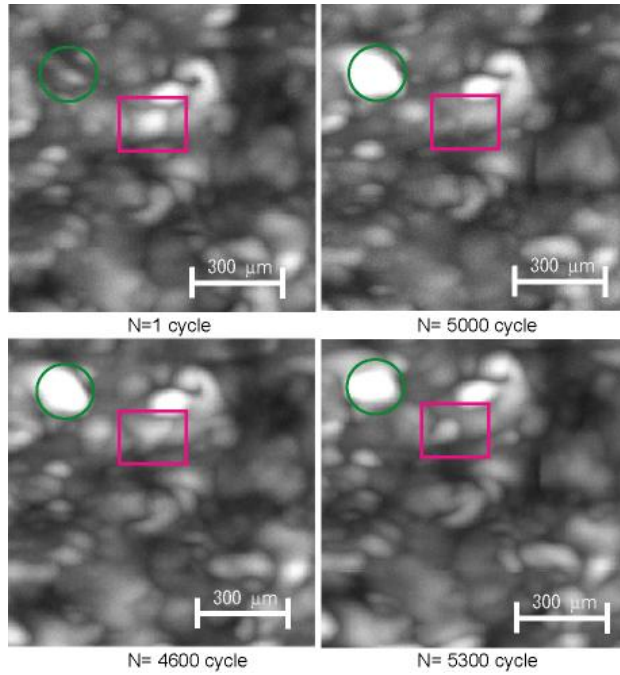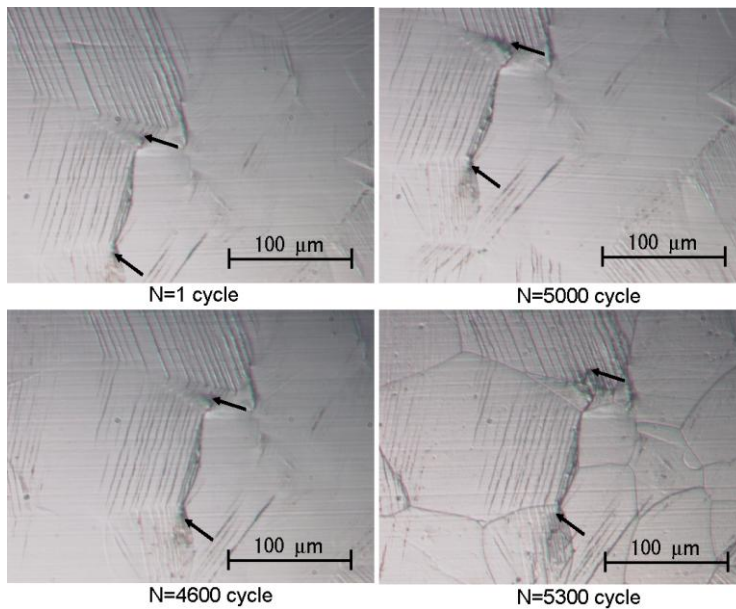

Fig.6. Scanning acoustic microscope images

Fig.7 Optical microscope images

4. Discussion

Fig. 6 shows that the back reflection intensity starts to decrease due to increase in cyclic loading and again start to increase. In corresponding optical microscope observations (Fig.7), we found that the length of the black line remains unchanged during ultrasonic decrease, but this black line length started to increase at the increase of back reflection intensity indicating the start of crack growth. Dislocation damping is considered as a major factor for such change in ultrasonic property. Due to the cyclic loading, dislocation density along persistent slip bands increase. The dislocation segments vibrate in response to ultrasonic stress wave and absorb the wave energy. To discuss the change in ultrasonic back reflection intensity due to cyclic loading, we will review the relationship between the dislocation density and attenuation. We assume a damage evolution model [15] in a crystal grain that includes PSBs relating D_{PSB} with plastic strain range and number of fatigue cycle.

$$D_{PSB} = \bar{D}_{PSB} \left[\left\{ 1 - \exp(-\kappa_{\varepsilon} \Delta \varepsilon_p) \right\} + \left\{ 1 - \exp(-\kappa_N \cdot \frac{N}{N_f}) \right\} \right] \quad N > 0 \tag{1}$$

where $\bar{D}_{PSB}$ is half the saturated value of D_{PSB}, κ_{ε} is a coefficient shows the dependency of D_{PSB} on the plastic strain amplitude, and κ_N is a coefficient shows the dependency of D_{PSB} on the number of cycles. The average dislocation density in the crystal grain including PSBs becomes

$$\Lambda_{av} = \Lambda_{PSB} \times D_{PSB} + \Lambda_0 \tag{2}$$

where Λ_{PSB} is the movable dislocation density in PSBs and Λ_0 is the initial dislocation density of the grain. Using the value of Λ_{av} from Eq.(2), we can estimate the ultrasonic attenuation in the grain including PSBs and the back-reflection intensity from the grain using [16, 17]

$$\alpha = C_1 \Lambda_{av} L^4 f^2 \tag{3}$$

$$\frac{A_{max}}{A_0} = \exp \left\{ -2(\alpha_1 - \alpha_0)H \right\} \tag{4}$$

where C_1 is the material constant, L is the dislocation loop length, f is the frequency of the ultrasonic wave, α_0 and α_1 are coefficients of attenuation for the initial and current states, respectively, and H is the radius of the crystal grain[15]. To calculate the attenuation using equation (3), we assume L, $\bar{\Lambda}_{PSB}$ and Λ_0 are 160 nm, $6.0 \times 10^{15} \, m^{-2}$ and $1.0 \times 10^{12} \, m^{-2}$ [18,19] respectively. The critical value of $\frac{A_{max}}{A_0}$ is assumed as the average amount of decrease in $\frac{A_{max}}{A_0}$ over several PSBs from where the crack growth starts in the experiment. The experimental and predicted values at start of crack growth using D_{PSB} model is shown in Fig. 8 and it is found that predicted value is close to the experimental value.
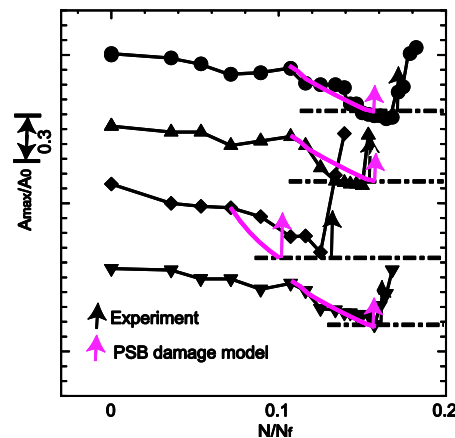

Fig.8. Relationship between back reflection intensity and fraction of fatigue life from simulation and experiment.

5. Conclusion

From this research it is found that the back-reflection intensity decreases with increasing the number of fatigue cycles before start of crack growth from PSBs. Monitoring this ultrasonic characteristic enables us to predict the remaining life of the fatigued stainless steel. The results obtained are summarized as follows;

1. Back reflection intensity from the boundary of grains where a PSB begins decreases at about 60% of the life of start of crack growth, until a large decrease about 30% occurs start of crack growth.

2. PSB damage evolution model can be used in order to predict the start of fatigue crack   growth under variable total strain range condition.

Acknowledgement

References

[1] Baniski, Z.S., Baniski, S.J., 1985. Low amplitude fatigue of copper single crystals—II. Surface observations, Acta Metallurgica, 33, p. 1307-1317.

[2] Ma, B. T., Larid, C., 1989. Overview of fatigue behavior in copper single crystals—I. Surface morphology and stage I crack initiation sites for tests at constant strain amplitude, Acta Metallurgica, 37, p. 325-336.

[3] Kim, W. H., Larid, C., 1978. Acta Metallurgica. 26, p. 777-787.

[4] Blochwitz, C., Richter, R., Tirschle, W., Obrtlik ,K., 1997. Materials   Science and Engineering. A234-236, p. 563-566.

[5] Davidson, D., Chan, K., McClung, S., Hudak, S., 2003. Small fatiue cracks. I. Milne, R.O. Ritchie, B. Karihaloo (Eds.), Comprehensive structural integrity. Vol.4 Amsterdam, Elsevier, p. 129-64.

[6] Man , J., Obrtlik, K., Blochwitz, C., Polak, J., 2002 Acta mater. 50, p. 3767-80.

[7] Polak, J., Man, J., Obrtik, K., 2003. AFM evidence of surface relief formation and models of fatigue crack nucleation. Int. J. Fatigue 25, p. 1027-1036.

[8] Man , J., Obrtlik, K., Polak, J., 2003. Study of surface relief evolution in fatigued 316L austenitic stainless steel by AFM, Materials Science and Engineering A, 351, p. 123-132.

[9] Hirao, M., Ogi, H., 1993. Fukuoka, Rev. Sci. Instrum. 64, p. 3198-3205.

[10] Truell, R., Hikata, A., 1957. ASTM STP No.213, Pennsyvania, USA, p. 63-77.

[11] Pawlowski, Z., 1963. Pr5oc. Vib. Prob. 4, p. 43-64.

[12] Tsuchida, Y., Okada, K., 1975. Bull. Fac. Eng., Tokushima Univ. 12, p. 31-42.

[13] Hirao, M., Ogi, H., Suzuki, N., Ohtani, T.,2000. Ultrasonic attenuation peak during fatigue of polycrystalline copper, Acta Materialia 48, p. 517-524.

[14] 'Stainless steel alloys specification'. JIS G4304, Japan Industrial Standard 2002.

[15] Islam, M.N., Arai, Y., 2009. Ultrasonic back reflection evaluation of crack growth from PSBs in low-cycle fatigue of stainless steel under constant load amplitude, Materials   Science and Engineering A 520, p. 49-55.

[16] Granato, A., Lücke, K., 1956. Theory of mechanical damping due to dislocations, Journal of applied physics 27, p. 583-593.

[17] Granato, A., Lücke, K., 1956. Application of dislocation theory to internal friction phenomena at high frequencies, Journal of applied physics 27, p.789-805.

[18] Wolfenden, A., 1983. Internal friction study of AISI 410 stainless steel, Scripta Metallurgica 17, p. 321-325.

[19] Bailat,   C., Groschel, F., Victoria, M., 2000. Deformation modes of proton and neutron irradiated stainless steels, Journal of Nuclear Materials 276, p. 283-288.